ARMY RESEARCH LABORATORY

In-Situ Measurement of Penetrator Erosion Rate and Dynamic Flow Stress During Long-Rod Penetration

Albert L. Chang

ARL-TR-1187 August 1996

NOTICES

REPORT DOCUMENTATION PAGE

Form Approved
OMB No. 0704-0188

1. AGENCY USE ONLY *(Leave blank)*	2. REPORT DATE	3. REPORT TYPE AND DATES COVERED
	August 1996	Final, Oct 92–Sep 94

4. TITLE AND SUBTITLE

In-Situ Measurement of Penetrator Erosion Rate and Dynamic Flow Stress During Long-Rod Penetration

5. FUNDING NUMBERS

312YN

6. AUTHOR(S)

Albert L. Chang

7. PERFORMING ORGANIZATION NAME(S) AND ADDRESS(ES)

U.S. Army Research Laboratory
ATTN: AMSRL-MA-PD
Aberdeen Proving Ground, MD 21005-5069

8. PERFORMING ORGANIZATION REPORT NUMBER

ARL-TR-1187

9. SPONSORING/MONITORING AGENCY NAME(S) AND ADDRESS(ES)

10. SPONSORING/MONITORING AGENCY REPORT NUMBER

11. SUPPLEMENTARY NOTES

12a. DISTRIBUTION/AVAILABILITY STATEMENT

Approved for public release; distribution is unlimited.

12b. DISTRIBUTION CODE

13. ABSTRACT *(Maximum 200 words)*

The penetration resistance of a given armor material against the long-rod projectile is primarily determined by its ability to erode away the projectile during the penetration process. Typically, high-energy X-Ray shadowgraphs were used to record projectile locations at different times after impact to calculate the projectile erosion rate. Due to the one-shot nature of the high-energy X-Ray equipment, this technique usually relies on combining multiple shadowgraphs taken from nominally "identical" ballistic experiments at different times after impact, introducing considerable uncertainties in the calculated erosion rates. In the present report, we describe the development of a 94-GHz CW Doppler Radar Hyper-Velocimeter system for *in-situ* and *continuous* measurement of the projectile tail-end velocity history. This radar system is capable of measuring both the magnitude and the direction of the velocity of a moving object. Signal processing algorithms were developed to extract the high-resolution tail-end velocity history from the Doppler frequency data. In the measured tail-end velocity history, several velocity-step changes are clearly visible. These velocity-step changes occur at specific times corresponding to stress wave reverberation along the projectile during the penetration process. Projectile length history (the erosion rate) was obtained by analyzing these velocity-step timing sequences. Tail-end position history was obtained by integrating the tail-end velocity history. Front-end position history was obtained through combination of the tail-end position history and the projectile length history. Dynamic flow stress of the projectile was obtained through the measurement of the size of the first velocity step in the tail-end velocity history. This dynamic flow stress represents the direct measurement of impact loading between two plastically deforming objects, i.e., the projectile and the target. Tail-end velocity history measurements of a 65-g 91W heavy metal projectile (with aspect ratio of 10) impacting an RHA block at several impact velocities provided the basis for calibrating dynamic material parameters used in model calculations.

14. SUBJECT TERMS	15. NUMBER OF PAGES
long-rod erosion rate, ballistics, dynamic yield strength	48
	16. PRICE CODE

17. SECURITY CLASSIFICATION OF REPORT	18. SECURITY CLASSIFICATION OF THIS PAGE	19. SECURITY CLASSIFICATION OF ABSTRACT	20. LIMITATION OF ABSTRACT
UNCLASSIFIED	UNCLASSIFIED	UNCLASSIFIED	UL

INTENTIONALLY LEFT BLANK.

ACKNOWLEDGMENTS

The author would like to express his thanks to his colleagues at the Materials Dynamics Branch, Army Research Laboratory, Materials Directorate, Watertown, MA: Mr. Raul Dominguez and Mr. John Loughlin for their efforts in the pusherless sabot design and its ballistic verification, Mr. Brian Durant for his assistance in collecting the radar signal data, Ms Luna Chiu for her CALE model calculations and Dr. Shun-chin Chou for his critical technical and administrative support. The Doppler radar was designed and built by Mr. Richard Pavadore at Engineering Specialties Service, Whitman, MA through Contract DAAL04-91-C-0081. Special thanks are reserved for Dr. Charles Anderson, Jr. at Southwest Research Institute, San Antonio, TX, for his CTH code calculations and useful discussions. This research program was initiated by the Inter Laboratory Innovative Research (ILIR) fund.

INTENTIONALLY LEFT BLANK.

TABLE OF CONTENTS

INTENTIONALLY LEFT BLANK.

LIST OF FIGURES

Figure | Page

LIST OF TABLES

INTENTIONALLY LEFT BLANK.

1. INTRODUCTION

The penetration resistance of a given armor material against a long-rod projectile is primarily determined by its ability to erode away the long-rod during the penetration process. After impact, the tail end of the rod typically travels at almost the original impact velocity while the front end of the rod, in contact with the target, advances at a lower velocity. Because of the velocity differential, the length of the rod decreases as it penetrates into the target. More effective target materials erode the rod at a higher erosion rate than less effective target materials. The target material and geometric properties responsible for eroding the rod (except for density) are generally termed the "target resistance." Although formulae exist for estimating the target resistance, it typically remains as a fitting parameter for model calculations. In the case of ceramic armor, due to damage of the ceramic material from impact, the target resistance may also depend on the physical constraint of the target system. Therefore, *in-situ* measurement of the projectile erosion rate and dynamic material properties are desirable to validate model calculations. High-energy X-Ray shadowgraphs are utilized for measurement of the projectile nose and tail positions at different times after impact, from which an erosion rate can be calculated. Although the high-energy X-Ray can see through the entire target assembly and it can obtain the image of the long-rod at that instant, this technique is limited by the one-shot nature of the high-energy X-Ray equipment. Therefore, this technique usually relies on combining multiple shadowgraphs taken from nominally "identical" ballistic experiments at different times after impact, introducing considerable uncertainties in calculating the projectile erosion rate. A lower energy X-Ray shadowgraph technique has also been used. Although the lower energy X-Ray equipment can take multiple shots of the same ballistic experiment at different times, this technique is limited by the amount of material that the x-rays can penetrate; therefore, this technique only works for non-prototypical systems with significantly reduced dimensions of the projectile and the target.

In the following sections, we will report the development of a new technique for determining the projectile erosion rate. This technique utilizes a 94-GHz Doppler radar which continuously measures the tail-end velocity of the projectile during penetration. From the measured velocity history, the projectile erosion rate and the dynamic flow stress can be obtained.

2. EXPERIMENTAL PROCEDURE

Three major developmental efforts were required to bring the experimental technique to fruition: 1) development of the 94-GHz prototype Doppler Radar Hyper-Velocimeter system with the capability to distinguish the projectile velocity signal from noise coming from debris; 2) development of a "pusherless sabot" package to launch the 1/4-scaled long-rod projectile without anything following the projectile such that the projectile was the only object moving away from the radar during the initial ~100 μs while the debris were moving toward the radar and 3) development of the signal processing algorithm and data analysis software to extract the tail-end velocity history and the projectile erosion rate from the Doppler frequency data.

2.1 Prototype Doppler Radar Hyper-Velocimeter. In the early stage of the development, it became apparent that the millimeter microwave system would have a distinct advantage over its laser counterpart for the velocity measurement in the ballistic range environment. Due to its longer wavelength (about 3 mm for 94 GHz), the microwave system did not require precision alignment and highly polished surfaces which were mandatory for the laser systems. Furthermore, the debris particles coming from ceramic armor during the penetration process obscure the laser beam but not the microwave beam. The schematic construction of the 94-GHz Doppler Radar Hyper-Velocimeter is shown in Figure 1. The VCO Gunn Oscillator (1) was the 94-GHz continuous wave (CW) microwave source. This reference microwave was divided into two parts through the 3 dB Coupler (2). Half of the original reference microwave was transmitted through the Waveguide Horn (4). The other half of the reference beam was further divided into two equal parts by a Power Divider (3) with a zero-degree phase delay in one and a 90-degree phase delay in the other. The returned signal, containing both the 94-GHz carrier wave and the Doppler signal, was collected by another Waveguide Horn (5) and it was divided into two equal parts by the Power Divider (6). They were combined with the two reference beams at the two Mixers (7 and 8) to eliminate the 94-GHz carrier wave and to provide the two intermediate frequency (IF) Doppler signals I (with zero-degree phase delay) and Q (with 90-degree phase delay). The I and Q signals were amplified by two Pre-Amps before being sent to the digital oscilloscope for analog-to-digital conversion and data storage. Combination of I and Q signals enabled one to obtain not only the magnitude of the velocity (Doppler frequency) but also the direction of the velocity whether the object was going away from the radar or coming toward the radar. Figure 2 shows a photograph of the 94-GHz Hyper-Velocimeter. Figure 3 illustrates the overall setup of the technique for the in-situ measurement of the long-rod projectile velocity history during penetration. The I and Q signals were digitized and stored in MS-DOS compatible format by a Nicolet Model 490E digital oscilloscope with two 200-MSamples/second 8-bit channels and two 10-MSamples/second 12-bit channels with 256kb memory per channel. The stored data were transferred to an MS-DOS compatible PC for post-test signal processing, using the software package Matlab and its signal processing toolbox from MathWorks.

2.2 Pusherless Sabot Development. A major effort was initiated to develop the "pusherless sabot" package to launch the 1/4-scaled tungsten heavy metal long-rod projectile with aspect ratio (L/D) 10 and 20. The original design came from the Ernst-Mach Institute in Freiburg, Germany, modified by Battelle Columbus (Goddard 1990), and modified further in the current effort for a powder gun with a 25-mm diameter smoothbore. Figure 4 shows a schematic representation of a pusherless sabot package. The main body of the sabot was made from aluminum which mated with the threaded long-rod. The aluminum sabot had four slits cut from the front end toward the rear along the longitudinal axis with a small amount of uncut material connecting these four quarters. After the threaded long-rod was placed into the aluminum sabot, a nylon bore rider, with several pre-cut notches to reduce its hoop strength, was placed at the front of the sabot to keep the four quarters tightly mated with the long-rod inside the bore. At the tail end, a nylon obtuator was mated with the aluminum sabot to serve as the gas seal. Two nylon sabot guides, occupying the empty space between the aluminum sabot and the bore, were used to prevent the premature disengagement of the long-rod from the aluminum sabot inside the barrel. During launching, the high gas pressure accelerated the obtuator which transferred the momentum to the aluminum sabot and the long-rod through the threads. After exiting the muzzle, the slitted bore rider broke apart, allowing the four quarters of the aluminum sabot to fly apart and disengaging the long-rod projectile. Figure 5 is a typical X-Ray shadowgraph showing sabot separation after exiting the muzzle. It was necessary to have a long flight path (>3 meters) to allow the aluminum sabot and the nylon obtuator to separate fully from the rod. With the nylon sabot guides in place to prevent premature disengagement of the projectile from the aluminum sabot, the nylon obtuator was designed to have just enough strength to withstand the high gas pressure loading inside the muzzle yet with reduced weight and pre-cut slits to make sure that it would be broken into several pieces after exiting the muzzle. These pieces tended to fly away from the projectile line-of-flight. An aluminum cone was threaded to the tail-end of the projectile to enhance its radar cross-section area.

2.3 Ballistic Range Setup and Timing Control. To protect the radar from being hit by the projectile or debris, it was necessary to place the radar vertically facing down such that the radar beams were perpendicular to the projectile line-of-flight. A U-shaped aluminum mirror was used to reflect the radar beams along the projectile flight path. The middle opening of the U-shaped mirror allowed the projectile to fly through while the two side arms of the mirror were used for reflecting both the transmitted and the received beams. No highly polished mirror surface was required. The radar hardware and its associated electronic components were protected between two steel blast plates. In order to minimize noise, a debris screen was placed between the armor target and the aluminum mirror. The front side of this debris screen facing the radar beam was covered with the radar-absorbing panel with a 7.62-cm hole cut out from it. Radar signals falling outside this hole were absorbed. Therefore, the received signal came only from the 7.62-cm circle target area centered at the point of impact, reducing the noise considerably. At the back side of the debris screen facing the target, a small battery-powered He-Ne laser and a photodiode served as the break-beam trigger for time-of-impact determination. The center of the laser beam was placed at a known distance from the surface of the target such that when the photodiode output was halved, the tip of the projectile was at the center of the laser beam. The time of impact is

then determined from the projectile velocity. Alternatively, the time of impact can be obtained directly from the sharp jump in the photodiode output produced by the impact flash. In a typical ballistic experiment, the radar system was first brought to a steady state. With the help of the micro-computer Real-Time controller developed by Chang et al. (Chang 1988), the trigger timing controls of the flash X-Ray tubeheads and the digital scopes for recording the I and Q channels and the laser-photodiode output at the correct times were accomplished automatically.

2.4 Signal Processing Algorithm Development. The Doppler radar output data (both I and Q) were recorded on MS-DOS compatible diskettes. A software program was written to translate the data from the Nicolet format to the Matlab MAT-file format. The sampling rate used was set at the maximum 200 MS/s, or sampling every 5 ns. For the current experiments, the total number of samples for I and Q channels were set to be 80,000 each. In other words, the elapsed time of data recording was set to be 400 μs.

Typically, for the size of the projectiles used, the penetration process of interest was expected to last for only about 100 μs. During the first 50 μs, the projectile velocity was not expected to vary much from the original launch velocity. Most of the projectile deceleration should occur in the latter 50 μs. It was recognized early in the development effort that the power spectrum analysis method using the sliding-window Fast Fourier Transform (FFT) algorithm was not useful since the current experiments demanded high resolution in both velocity and time, which was impossible for the slide-window FFT methods. In other words, if one used the sliding-window FFT method and demanded a high time resolution by choosing a narrow window in time domain, the velocity resolution (in frequency domain) would be lowered significantly, and vice versa.

A new signal processing algorithm called Moiré Fringe method has been developed, which can provide the velocity history of the projectile with high resolution in both velocity and time. This method is based on the principle of Moiré interference fringes. If the signal collected from the current experiments had relatively low noise, it would be very close to a perfect sinusoidal wave with Doppler frequency decreasing with time. For illustration purposes, assume that the original free-flight frequency was at 0.99 MHz; i.e. the original signal had a 1.01-μs period. If one plotted the data by skipping every 0.5 μs (corresponding to a perfect sinusoidal wave at 1 MHz), a Moiré interference pattern would appear as shown in Figure 6 (solid line). This Moiré pattern is due to the interference between the reference wave (the perfect sinusoidal wave at a fixed 1-MHz frequency) and the measured wave whose frequency decreases from the original 0.99 MHz with time. If the original data is plotted with a skip-time of 1.0 μs (instead of 0.5 μs), an envelope wave of the Moiré pattern will result (the Envelope1 curve in Figure 6). Furthermore, if plotting is started 0.5 μs later with the same 1.0 μs skip-time, a complementary envelope wave (the Envelope2 curve) will result as shown in Figure 6. These two complementary envelope waves define a series of intersections. The frequency of the Moiré pattern can be determined from the time difference between these intersections with high accuracy due to the fact that a small difference in frequency domain corresponds to a large period in time domain. Each Moiré frequency (or velocity) is assigned a time corresponding to the middle of the time interval defined

by these intersections. The Moiré frequency ($F_{moiré}$) represents the difference between the reference frequency (F_{ref}) (1 MHz, due to the 0.5-μs skip-time) and the actual projectile frequencies (F_{actual}) (0.99 MHz and lower), therefore, the actual projectile frequency (or velocity) at this time instance can be obtained through: $F_{actual} = F_{ref} - F_{moiré}$, as illustrated in Figure 7. The previous procedure is repeated with a slightly later starting time until the entire time history is completed. Although the maximum Doppler frequency expected from our current experiments was at about 1 MHz, our sampling rate was set at 200 MHz. This over sampling was necessary to obtain high time resolution of the velocity history using the Moiré Fringe method.

Since the Moiré Fringe method demands a relatively clean signal, it was necessary to separate the signal (coming from the projectile) from the noise (coming from the debris). This procedure is accomplished by the power spectrum analysis method using the FFT algorithm which converts the original I and Q data from the time domain to the frequency domain. The FFT procedure separates the signal into positive frequencies (debris velocities coming toward the radar) and negative frequencies (projectile velocities going away from the radar). By setting the power spectrum of the positive frequencies to zero and performing the inverse FFT (IFFT) procedure, a new set of I and Q time domain data, free of the noise coming from the debris, can now be processed using the Moiré Fringe method to obtain the projectile velocity history. The FFT-IFFT procedure and the Moiré Fringe method were implemented in several Matlab script files on an MS-DOS PC.

3. EXPERIMENTAL RESULTS

3.1 Projectile Velocity History. Ballistic experiments were conducted to develop the projectile velocity history measurement technique. The projectile was a modified 1/4 scale 91W tungsten heavy metal projectile with L/D=10 hitting a 127-mm-thick RHA block at various impact velocities. The projectile had a 5.1-cm-long thread from the back to mate with the threaded aluminum sabot. An aluminum cone was threaded at the end of the projectile to enhance its radar cross-section. It was found that the 60-mw radar had more than enough power to measure the velocity history of the projectile since the distance from the radar to the surface of the armor target was only about 1 m. Figure 8 shows the measured projectile tail-end velocity history using the Moiré Fringe method as described in the previous section using a Moiré skip-time of 0.51 μs. Since the data obtained from this particular experiment (test T55-92-7) were relatively clean, the I channel time domain data were used directly without the FFT-IFFT cleanup procedure. Several different Moiré skip-times around 0.5 μs were tried, and they all show consistently the same velocity history with varying degrees of velocity resolution. In general, if the reference frequency was set too far above or too close to the actual measured frequency, the noise in the measurement sometimes gave rise to erroneous "velocity gaps." When the reference frequency was set at an appropriate level just above the actual frequency, the velocity history curve became smoother without the gaps. The Moiré frequency increases with time, corresponding to the slowing down of the projectile.

Several interesting features in Figure 8 should be pointed out. Firstly, the velocity history is very noisy approximately 60 μs after impact. Closer examination of the original time domain data indicated that the Doppler signal vanished after ~60 μs. This is believed to be due to the fact that at this time, the tail end of the projectile had traveled ~8.9 cm from its position at impact, i.e. the 7.42-cm-long projectile had penetrated inside the RHA target, with the tail being ~1 cm inside the target surface, making the tail invisible to the radar due to geometry. Therefore, the velocity history shown in Figure 8 is truncated.

Secondly, there was a slight increase in projectile velocity during the free-flight part of the history. Careful examination of the system setup indicated that this slight increase in velocity was due to the decreasing angle between the projectile line of flight and the line joining the tail end and the radar receiving horn when the projectile was moving away from the radar. This geometric dependence confirmed the fact that our velocity measurement technique had excellent velocity resolution.

Thirdly, it was noted that at around 19 μs after impact, the velocity decreased in a small but noticeable step change. The time for the velocity-step change was taken at where the slope of the velocity-time curve begins to change. A similar step change in velocity, albeit less obvious, was also noticed at around 45 μs. These velocity-step changes were thought to be due to a stress wave generated by the initial impact propagating along the projectile and reflected back and forth between the front-end and the tail-end interfaces. Every time the stress wave reflected from the

tail-end free surface, a velocity-step reduction was produced. In other words, the stress wave could serve as an indicator to sample the current length of the projectile during the penetration process. Numerical simulation confirmed the existence of these velocity steps. Furthermore, the calculated time sequence of these velocity steps suggested that the time intervals between these velocity steps obeyed a geometric relationship with the length change history (or the erosion rate) of the long-rod projectile.

3.2 Projectile Erosion Rate. The relationship among successive time intervals between the velocity steps can be derived from simple geometric consideration such that:

$$t_1 - t_0 = L(t_0) / C;$$

$$t_3 - t_1 = 2L(t_2) / C = \{2L(t_0) / C\}*\{(C - E_{20}) / (C + E_{20})\};$$

$$t_5 - t_3 = 2L(t_4) / C = \{2L(t_0) / C\}*\{(C - E_{20}) / (C + E_{20})\} *\{(C - E_{42}) / (C + E_{42})\};$$

$$t_7 - t_5 = 2L(t_6) / C = \{2L(t_0) / C\}*\{(C - E_{20}) / (C + E_{20})\} *\{(C - E_{42}) / (C + E_{42})\} *\{(C - E_{64}) / (C + E_{64})\};$$

. . .

Equation (1)

where

$t_{i=even}$	=	time after impact when the stress wave is at the front end of the projectile
$t_{i=odd}$	=	time after impact when the stress wave is at the tail end of the projectile
$L(t_i)$	=	projectile length at time t_i
C	=	stress wave velocity inside the projectile
E_{ij}	=	averaged projectile erosion rate between t_i and t_j

After the impact at t_0, one branch of the stress wave generated at the projectile/target interface propagates toward the tail end of the projectile while the other propagates toward the back side of the target. When the stress wave reaches the tail end (at t_1), the particle velocity at the tail end is reduced abruptly by the stress wave, giving rise to a velocity-step change which is measured by the Doppler radar tracking the tail-end velocity history. This stress wave is reflected from the tail-end free surface and propagates toward the front end of the rod. When it reaches the front end (at t_2), the length of the projectile has been reduced by erosion to $L(t_2)$. This wave is again reflected toward the tail end, traveling the length $L(t_2)$ again. When it reaches the tail end (at t_3), a second velocity-step change occurs. This second velocity-step change is smaller and

the change becomes more continuous than the first velocity-step change. The reverberation of this stress wave continues and each successive step becomes less observable. On the other hand, the other branch of the original stress wave propagating toward the back side of the target block is reflected at the back surface and toward the projectile/target interface. Part of this reflected wave also propagates toward the tail end, giving rise to a possibly different set of velocity steps. Therefore, it was advisable to use a thick target block in order not to confuse these multiple sets of velocity-step signals.

Figure 9 shows the zoom-in version of the tail-end velocity history for test T55-92-7 with Moiré skip-time = 0.51 μs and V_p = 1481 m/s (same as Figure 8). The velocity steps are marked at t_1 = 18.8 μs and t_3 = 44.6 μs. It was not possible to observe the third velocity step at t_5 due to the interference between the aluminum cone and the cavity during penetration, giving rise to a sharp drop in the velocity history around t = 55 μs.

In order to obtain more complete sets of velocity steps to verify the above procedure for erosion rate determination, additional ballistic tests at lower projectile velocities were performed with the same L/D=10 projectile. The measured velocity histories are shown in Figure 10 (test T5-93-6, V_p = 1228 m/s, Moiré skip-time = 0.61 μs), Figure 11 (test T5-93-7, V_p = 957 m/s, Moiré skip-time = 0.78 μs) and Figure 12 (test T5-93-9, V_p = 789 m/s, Moiré skip-time = 0.95 μs). The time sequence of the velocity step changes are marked in these figures. These velocity-step sequences were determined by visual examination of the abrupt slope changes in high-resolution velocity history plots.

Table I summarizes the results of the erosion rates obtained from these velocity histories using Equation (1). Note that the erosion rate was decreasing slightly with penetration time. Furthermore, the erosion rate appears to be velocity independent, constant at the averaged level of 765 m/s.

Although the current experimental procedure did not allow direct measurement on the front-end velocity history, it was possible to obtain the projectile front-end position at t_0, t_2, t_4 ... etc. from the measured tail-end velocity history and from the projectile length information, $L(t_0)$, $L(t_2)$, $L(t_4)$, ... obtained from the measured velocity-step time sequence. By integrating the tail-end velocity history, the tail-end position history was obtained. The front-end position at t_i was simply the sum of the current projectile length $L(t_i)$ and the tail-end position at t_i.

3.3 Dynamic Flow Stress. According to Anderson et al. (Anderson 1991), the dynamic flow stress of the projectile, Y_p, is related to the particle velocity-step reduction, ΔV, by:

$$Y_p = (\Delta V \rho_o C)/2 \qquad \text{Equation (2)}$$

where

Y_p = dynamic flow stress of the projectile
ΔV = velocity-step reduction
ρ_o = density of the projectile
C = bar wave speed of the projectile

Using the measured values of ΔV with $\rho_o = 17.4$ g/cm^3 for 91W tungsten heavy alloy and C = 4220 m/s, the dynamic flow stress of the 91W tungsten heavy alloy at various projectile velocities were obtained using Equation (2) and tabulated in Table II. Notice that the calculated dynamic flow stress is higher at higher velocities. The current experimental technique and analytical procedure, for the first time, provided independent measurements of dynamic flow stress of the 91W tungsten heavy alloy projectile with L/D=10 at various impact velocities against the same RHA block target.

The dynamic flow stress measured from the velocity step size was used in the subsequent Tate model calculations as Y_p. As shown in Table II, Y_p was found to be dependent on the projectile velocity. In all the Tate model calculations, the target resistance was chosen to be $R_t = Y_p + 2.94$ GPa as suggested by Anderson et al. (Anderson 1991). No attempt was made to optimize the choice of R_t.

4 COMPARISON WITH MODEL CALCULATIONS

The current experiment offered a unique opportunity to verify various model calculations. Early calculations were performed by the CALE code to confirm the velocity-step time sequence. Later efforts included more detailed comparison with the Tate model and CTH code calculations. In these efforts, the lowest velocity experiment (test T5-93-9, V_p = 795 m/s) was chosen to be the case for detailed comparison because this test had the most complete velocity-step sequence in the measured velocity history. The depth of penetration (DOP) in the RHA block was also measured.

4.1 CALE Code Calculations. This early code calculation was performed to confirm the timing of the observed velocity-step time sequence. This was the basis for the geometric relationship expressed in Equation (1). The CALE code calculation also suggested that the observed velocity-step sequence was cut short by the formation of the impact cavity in the RHA block which interfered with the radar signal. This analysis led to additional ballistic experiments at lower velocities to obtain more complete velocity-step time sequences.

4.2 CTH Code Calculations. Figure 12 shows the measured projectile tail-end velocity (T5-93-9, Vp = 789 m/s) as compared to the calculated history by using the CTH code. This calculation was performed by Anderson at the Southwest Research Institute (Anderson 1994). The velocity step changes were very visible in the calculated history. The observed velocity steps were much broader and less well-defined than those from the calculation. In general, the agreement in the velocity-step timing sequence was excellent between the CTH code and the measurement. Figure 13 shows the comparison between the CTH-calculated and the measured projectile tail-end position history and the front-end position history. The agreement in tail-end position history was excellent. The fairly large disagreement in the tail-end position history after 120 μs should be ignored since the Doppler radar signal vanished after about 110 μs. Using the measured DOP as the reference for judging the predicted front-end position histories, the CTH code slightly over-predicted the front-end positions while the velocity-step procedure under-predicted the front-end positions. The possible explanation for this under-production will be discussed later.

4.3 Tate Model. The one-dimensional model proposed by Tate (Tate 1967) has become the standard reference for long-rod penetration of thick targets in the velocity regime where projectile erosion is of interest. It should be pointed out that the front-end and tail-end position of the projectile obtained from numerical integration of the Tate model depends critically on the choice of the dynamic flow stress of the projectile Y_p, and the target resistance R_t. There were no *a priori* procedures to determine these parameters. They were usually treated as adjustable parameters to fit the observed DOP data. Figure 14

shows the comparison between the calculated (Tate model) and measured projectile tail-end velocity history for test T55-92-7 (V_p = 1481 m/s) with the dynamic flow stress Y_p = 2.19 GPa and the target resistance R_t = 5.08 GPa. Figure 15 shows the comparison between the calculated (Tate Model) and measured front-end and tail-end position history for test T55-92-7 (V_p = 1481 m/s) with the same Y_p and R_t. Figure 16 shows the comparison between the calculated (Tate model) and measured projectile tail-end velocity history for test T5-93-6 (V_p = 1228 m/s) with the dynamic flow stress Y_p = 1.62 GPa and the target resistance R_t = 4.62 GPa. Figure 17 shows the comparison between the calculated (Tate Model) and measured front-end and tail-end position history for test T5-93-6 (V_p = 1228 m/s) with the same Y_p and R_t. Figure 18 shows the comparison between the calculated (Tate model) and measured projectile tail-end velocity history for test T5-93-7 (V_p = 957 m/s) with the dynamic flow stress Y_p = 1.57 GPa and the target resistance R_t = 4.56 GPa. Figure 19 shows the comparison between the calculated (Tate Model) and measured front-end and tail-end position history for test T5-93-7 (V_p = 957 m/s) with the same Y_p and R_t. Figure 20 shows the comparison between the calculated (Tate model) and measured projectile tail-end velocity history for test T5-93-9 (V_p = 789 m/s) with the dynamic flow stress Y_p = 1.56 GPa and the target resistance R_t = 4.51 GPa. Figure 21 shows the comparison between the calculated (Tate Model) and measured front-end and tail-end position history for test T5-93-7 (V_p = 789 m/s) with the same Y_p and R_t.

5. DISCUSSION

5.1 Techniques and Procedures. It should be pointed out that projectile tail-end velocity histories with various velocity-step changes occurring at different times can only be measured using a *continuous* measurement technique (such as the current one) with sufficient resolutions both in the time domain and in the velocity domain. There was a wealth of information on projectile/target interaction embedded in these velocity histories not obtainable via X-Ray shadowgraphs.

The Doppler radar proved to be reliable and can be set up easily in any ballistic range. On the other hand, to obtain an optimal pusherless sabot design for various projectiles required significantly more effort. The aluminum cone attached at the tail end of the L/D=10 projectile was found to be essential to achieve a high signal-to-noise ratio in the Doppler signal received. Doppler signals returned from L/D=20 projectiles without the aluminum cone were too noisy to reveal the velocity steps in the velocity history.

The software algorithms for implementing the Moiré Fringe method developed to obtain the velocity history from the I & Q Doppler signals proved to be highly successful with sufficient resolution both in velocity and in time. However, it is noted that although the Moiré Fringe method provides high resolution in relative time, there is an uncertainty in absolute time. This is due to the rather arbitrary assignment of the time, which was set to be at the middle of the interval defined by intersections of the two envelope waves (see Figure 6). In the velocity-step timing analysis for erosion rates, the time-of-impact, t_0, was adjusted to be consistent with the stress wave speed C. Time intervals between t_1 and t_3, t_3 and t_5, t_5 and t_7 ... were not adjusted and the measured erosion rates E_{20}, E_{42}, E_{64} ... were independent of t_0.

5.2 Front-End Position History. Although the current experimental technique provides the direct measurement on the tail-end velocity history only, analytical procedures were developed to obtain the dynamic flow stress, the projectile erosion rate, and the front-end position history from the tail-end velocity history.

The front-end velocity (or the interface velocity) is defined to be: $V_i(t) = V_p(t) - E(t)$ where $V_p(t)$ is the tail-end velocity history and E(t) is the erosion rate. $V_i(t)$ is determined by the relative dynamic strength of the projectile with regard to the target. $V_p(t)$ is fairly close to the initial projectile velocity for the majority of the duration of the penetration process. The data in Table I indicate a fairly constant erosion rate at ~765 m/s for all ballistic tests, independent of impact velocity, investigated in this effort. Higher initial projectile velocity contributes to a higher front-end velocity and, therefore, larger penetration.

In all Tate model calculations (Figure 15, 17, 19, and 21), the agreement in the front-end position history was excellent, except in the case of test T5-93-9 (V_p = 789 m/s), where the Tate mode over-predicted the initial penetration and correctly predicted the DOP (see Figure 21). CTH model calculations of test T5-93-9 (V_p = 789 m/s) slightly over-predicted both the initial penetration and the DOP while the velocity-step procedure significantly under-predicted the front-end positions (see Figure 13). Since the observed velocity-step timing sequence agreed with the CTH model calculation result fairly well (see Figure 12), it seemed that the under-prediction in the front-end positions was due to something more fundamental in nature. In the current analytical procedures, projectile lengths were calculated from the observed velocity-step sequence based on the assumption that the stress wave reverberating back and forth along the projectile was traveling the entire length of the projectile. In view of the results in Figure 12 and 13, it seemed that this assumption was not valid. It was suggested by Anderson (Anderson 1994) that there exists an elastic/plastic interface near the front end of the projectile. The majority of the projectile remained undeformed (elastic zone) while the mushroom-head was severely deformed (plastic zone). After the stress wave was reflected from the free surface at the tail end, it was again reflected at the plastic/elastic interface, not at the projectile/RHA interface. In other words, there seemed to be a plastic zone (~1-projectile-diameter-long mushroom-head) near the front end of the projectile. Some residual projectiles were recovered after impact. The mushroom-head was measured to be ~0.85 cm in length. Assuming this mushroom-head remained constant in length soon after it was formed by initial impact, one can adjust the front-end positions obtained by velocity step by a constant 0.85 cm (shown as hollow squares in Figure 13). These adjusted front-end positions are closer to the observer DOP data. The formation of the plastic zone and the premature reflection of the elastic wave at the elastic/plastic interface should also be present in the higher velocity cases. Therefore, it is suggested that the apparent erosion rate is slightly larger due to the exclusion of the mushroom-head length from the stress wave reverberation path length.

6. CONCLUSIONS

In previous sections, we have described the development of a 94-GHz CW Doppler radar system and the signal processing algorithm capable of measuring the projectile tail-end velocity history with high resolution both in time and in velocity, such that fine features of the stress wave reverberation during the penetration process can be detected and used to determine the projectile erosion rates and the dynamic flow stress. Specifically, we conclude that:

1. A 94-GHz CW Doppler radar system was developed with I and Q channels capable of measuring both the magnitude and the direction of the velocity of a moving object.

2. With the implementation of the Moiré Fringe method inside the signal processing procedure, the velocity history of the projectile tail end can be obtained from the time domain data with high resolution both in velocity and in time.

3. Stress wave reverberation inside the projectile rod during the penetration process was observed with the radar system. Projectile erosion rates can be obtained directly from the timing information of these reverberations.

4. Dynamic flow stress of the 91W tungsten heavy alloy 1/4-scale long-rod projectile at various projectile velocities against the RHA target was independently obtained from the velocity-step size analysis.

7. REFERENCES

Anderson, C. E. Jr. and Walker, J. D. "An Examination of Long-Rod Penetration", Int. J. Impact Engng . Vol 11, No. 4, 481-501 (1991).

Anderson, C. E. Jr. private communication (1994).

Chang, A. L., Vincent, P. M. and Martorell, I. A. "Microcomputer Real-Time Flash X-Ray Controller", Proceedings of 39th Meeting of the Aeroballistic Range Association, Albuquerque, NM (1988).

Goddard, S. "Development of Reliable, Inexpensive Sabots", Proceedings of 41st Meeting of the Aeroballistic Range Association, San Diego, CA (1990).

Tate, A. "A Theory for the Deceleration of Long-rods after Impact", J. Mech. Phys. Solids 15, 287-399 (1967).

Table I. Erosion Rates Obtained From Projectile Tail-End Velocity-Step Sequence

Test No.	T55-92-7	T5-93-6	T5-93-7	T5-93-9
V_p (m/s)	1481	1228	957	789
t_1 (μs)	18.8	18.4	18.8	18.8
t_3 (μs)	44.6	43.9	46.7	45.3
t_5 (μs)			63.1	64.1
t_7 (μs)			77.6	77.8
t_2 (μs)	31.7	31.1	32.0	32.0
t_4 (μs)			53.8	54.7
t_6 (μs)			70.3	71.0
$L(t_0)$ (cm)	7.920	7.755	7.940	7.938
$L(t_2)$ (cm)	5.453	5.380	5.451	5.583
$L(t_4)$ (cm)			3.881	3.983
$L(t_6)$ (cm)			3.061	2.891
E_{20} (m/s)	778.8	762.6	784.9	734.9
E_{42} (m/s)			709.0	706.5
E_{64} (m/s)			500.2	666.9

Table II. Dynamic Flow Stress Y_p Obtained From Tail-End Velocity-Step Change

Test No	T55-92-7	T5-93-6	T5-93-7	T5-93-9	CTH
V_p (m/s)	1481	1228	957	789	795
ΔV (m/s)	59.6	44.2	42.6	42.5	46.6
Y_p (GPa)	2.19	1.62	1.57	1.56	1.71
R_t (GPa) (Tate)	5.08	4.62	4.56	4.51	N/A
DOP (cm)	N/A	N/A	2.637	1.280	1.643

94-GHz Hyper-Velocimeter

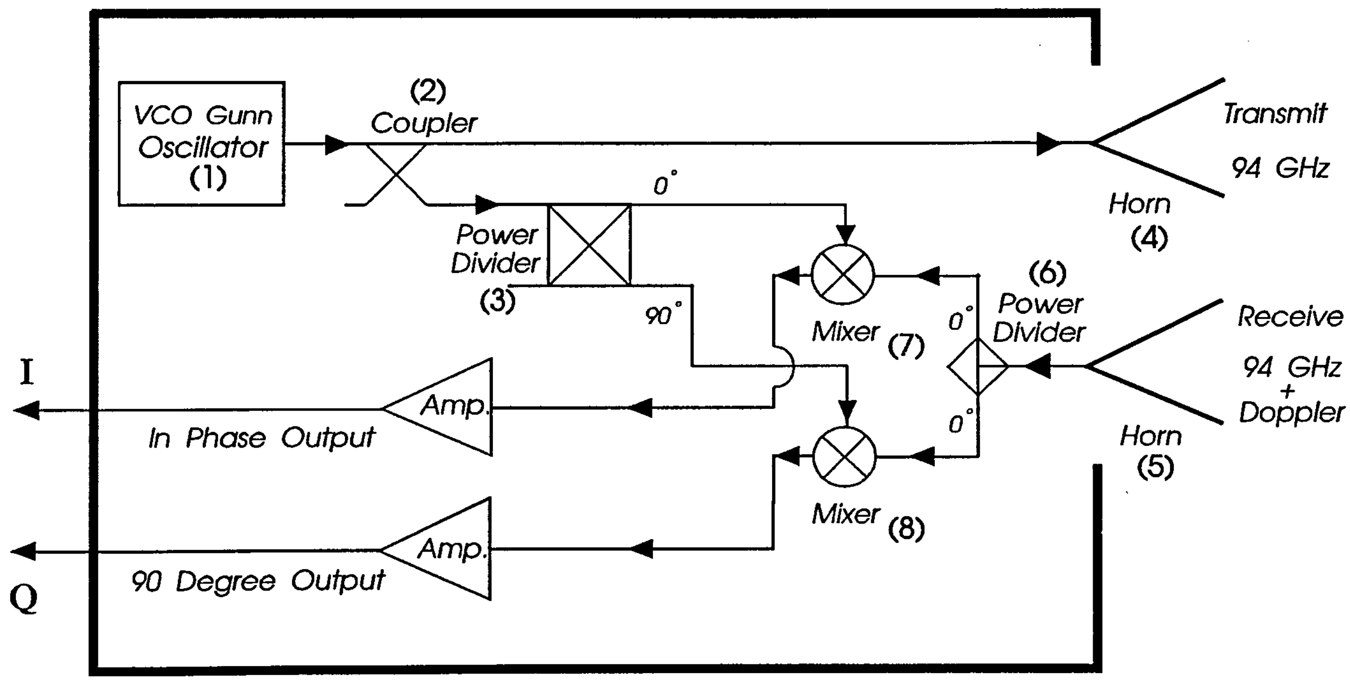

Figure 1. Schematic of a 94-GHz Doppler Radar Hyper-Velocimeter

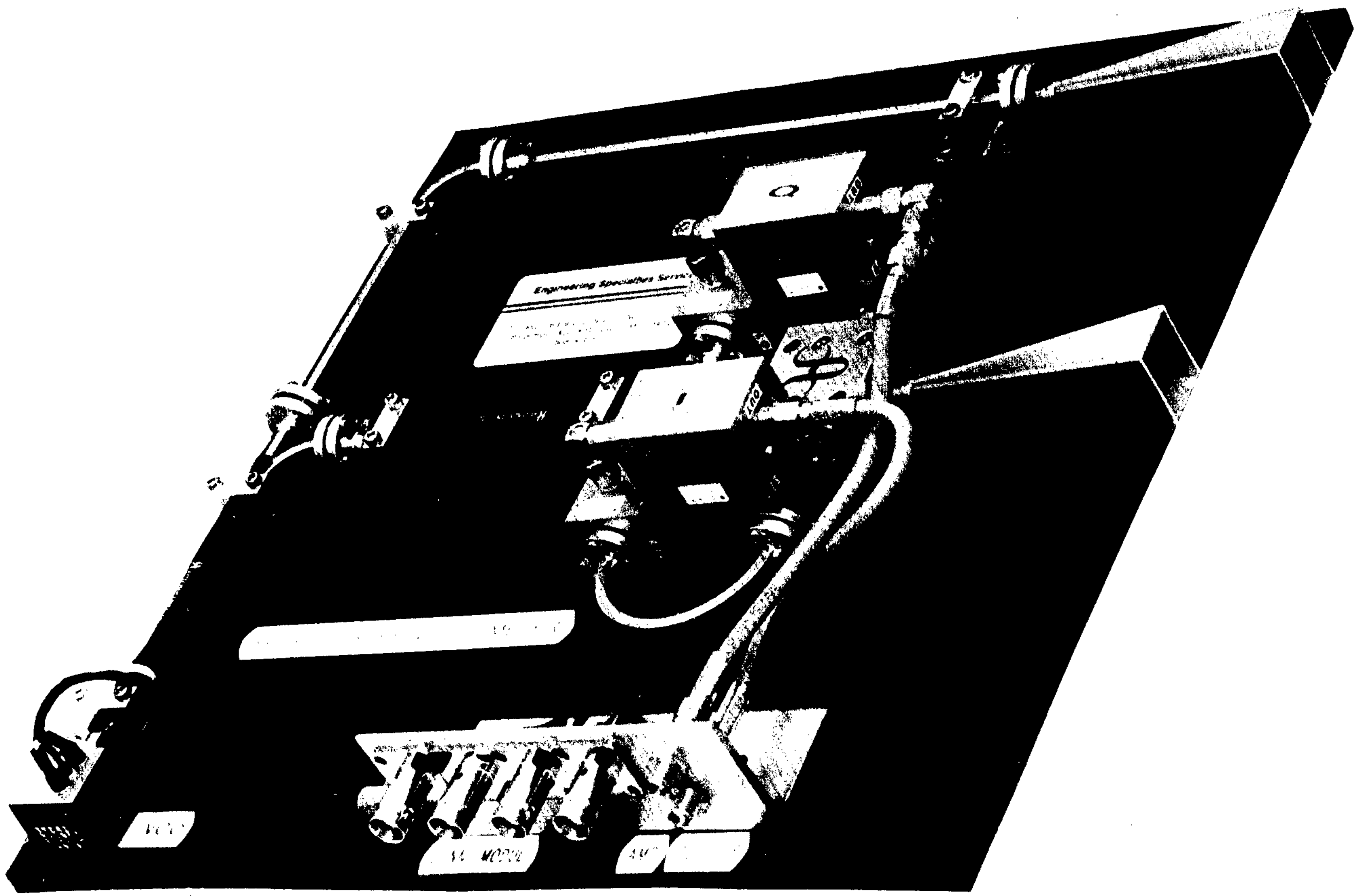

Figure 2. A 94-GHz Doppler Radar Hyper-Velocimeter

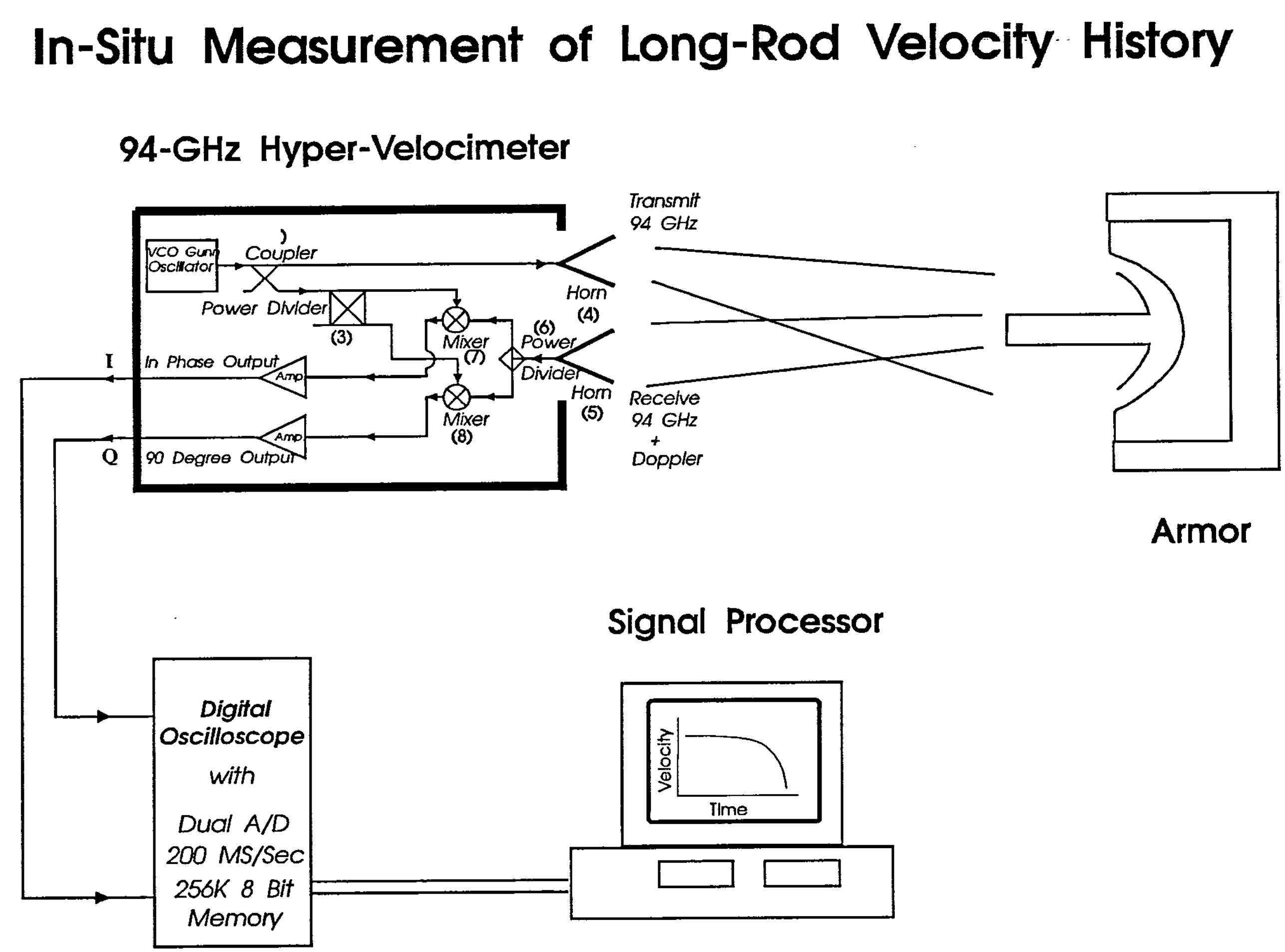

Figure 3. Schematic overview of the experimental setup for in-situ measurement of projectile tail-end velocity history

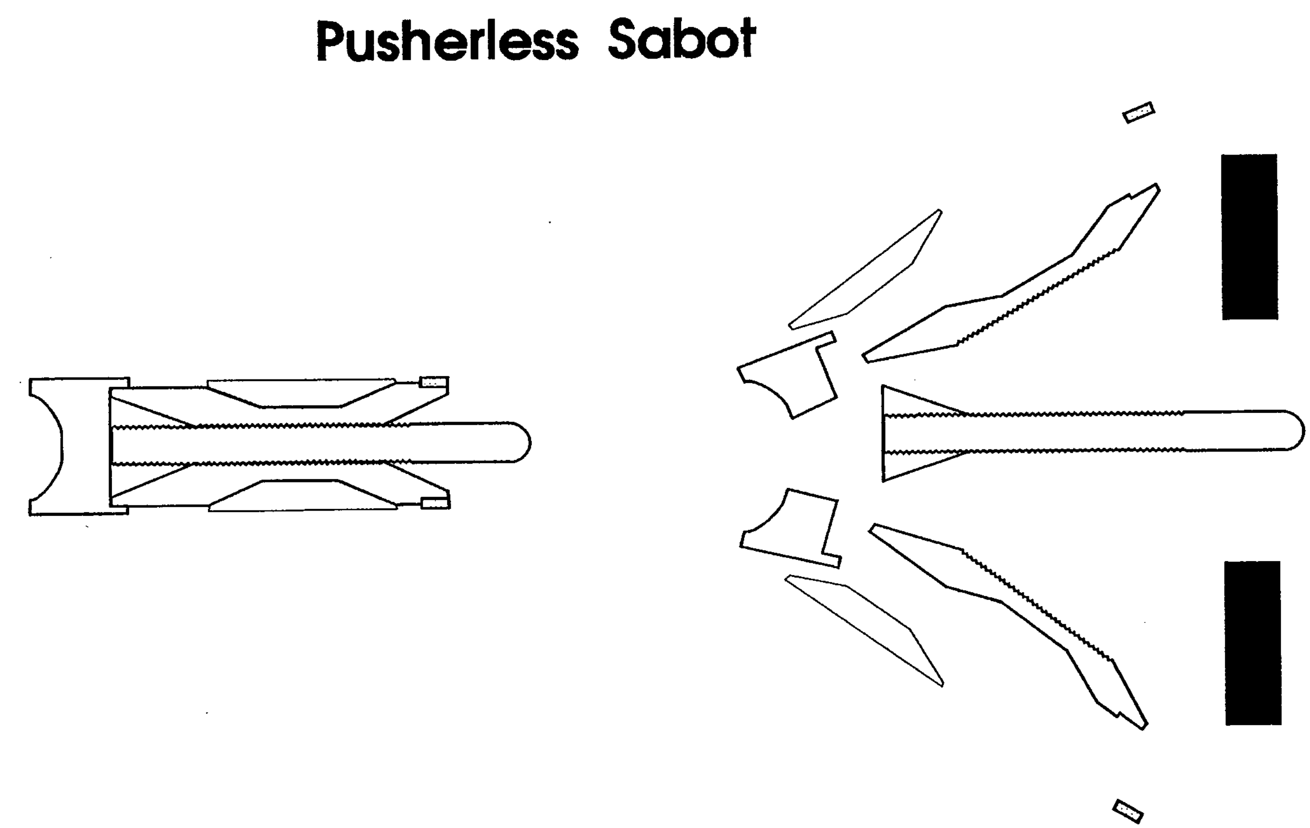

Figure 4. Schematic of a pusherless sabot long-rod penetrator package

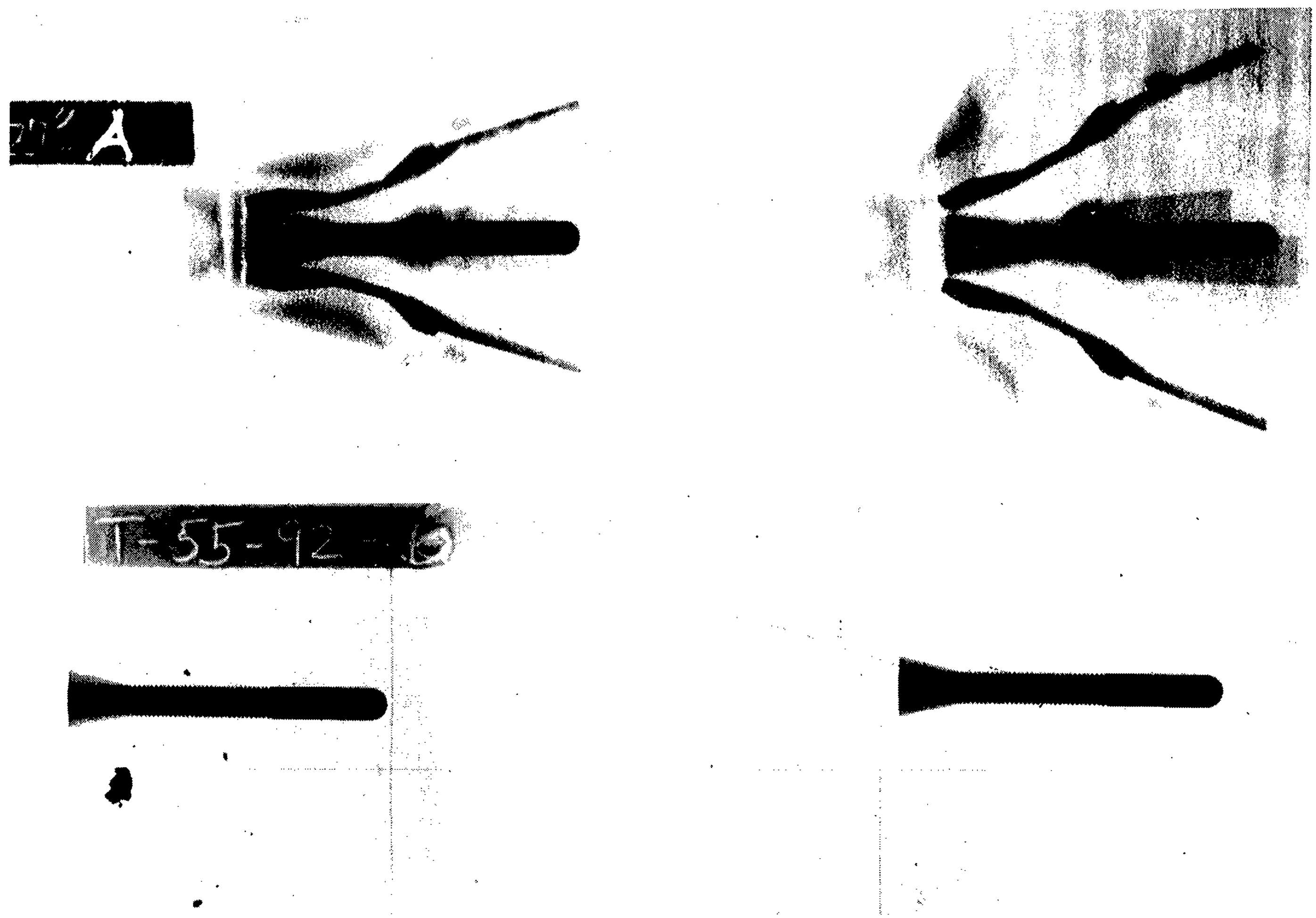

Figure 5. A typical X-Ray shadowgraph showing the pusherless sabot separating from a long-rod penetrator

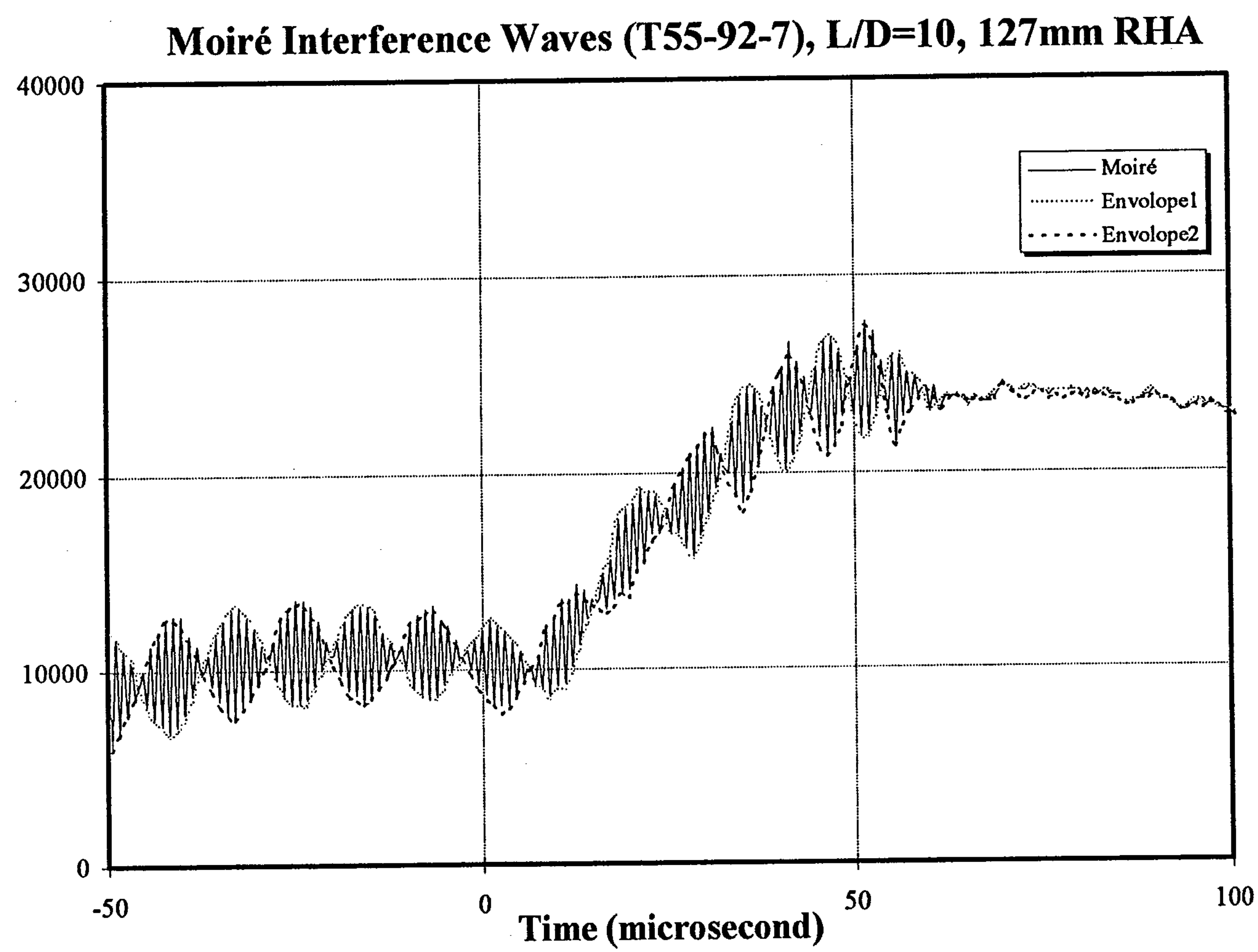

Figure 6. A Moiré interference pattern obtained when plotting the time domain data skipping every 0.51 μs

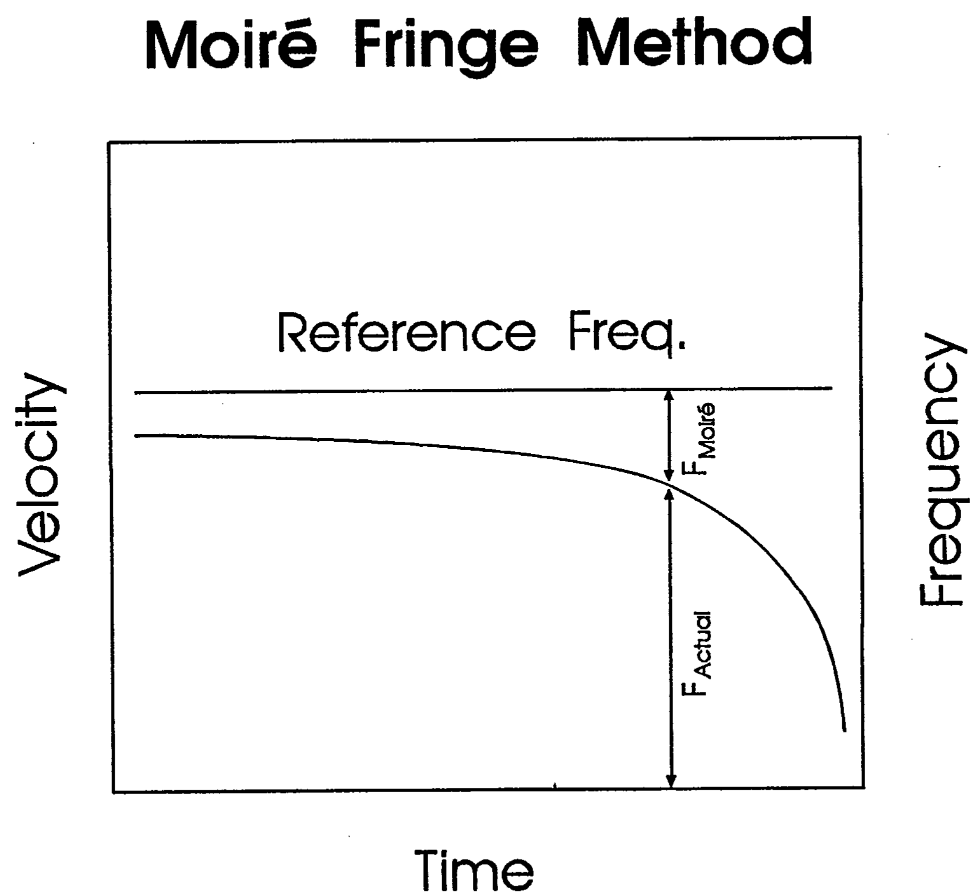

Figure 7. Illustration of the Moiré Fringe Method Factual = Fref - Fmoiré

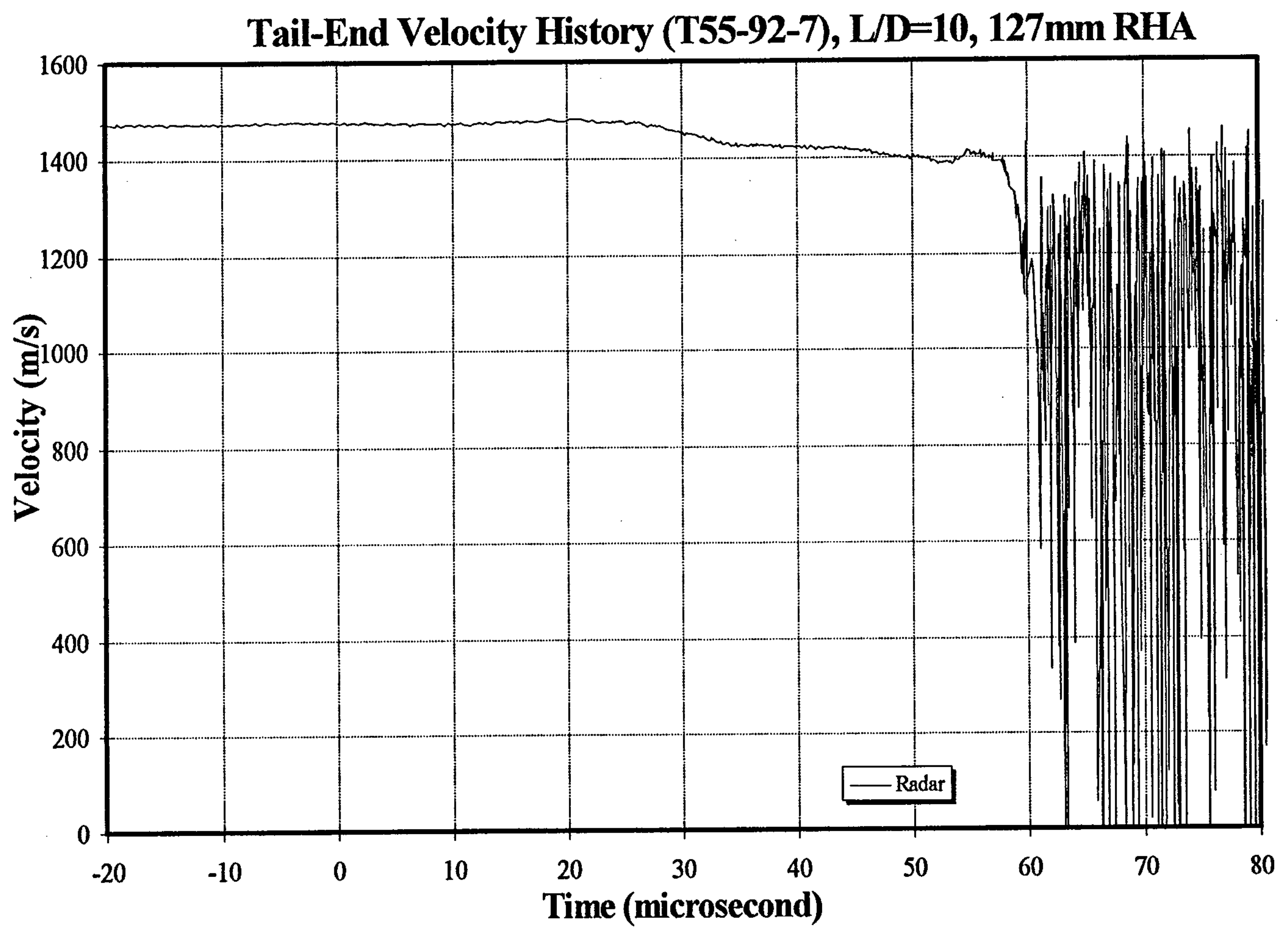

Figure 8. Tail-end velocity history for test T55-92-7 obtained by using the Moiré Fringe method with a 0.51-μs skip-time

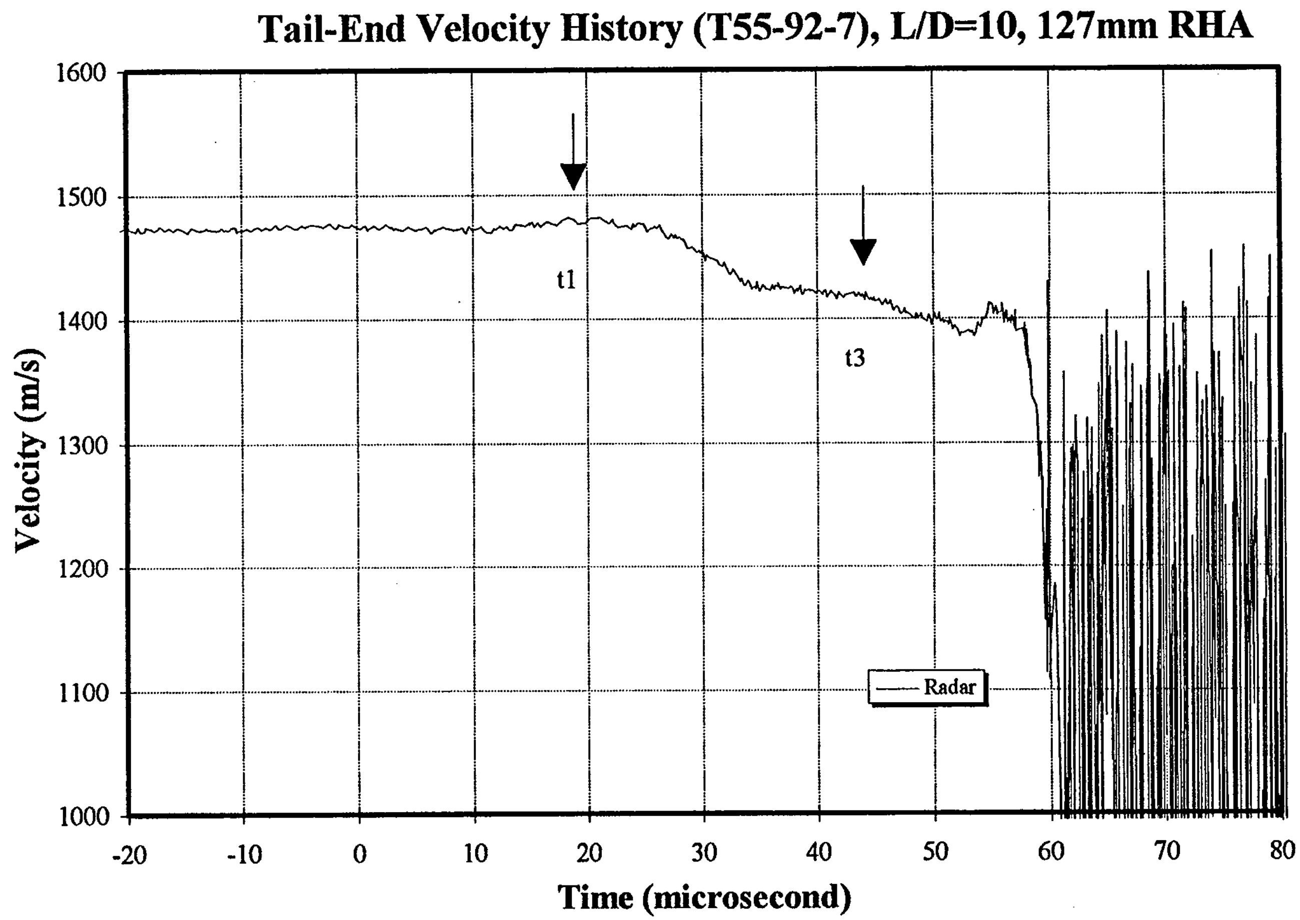

Figure 9. Tail-end velocity-step changes and corresponding time sequence marked (test T55-92-7)

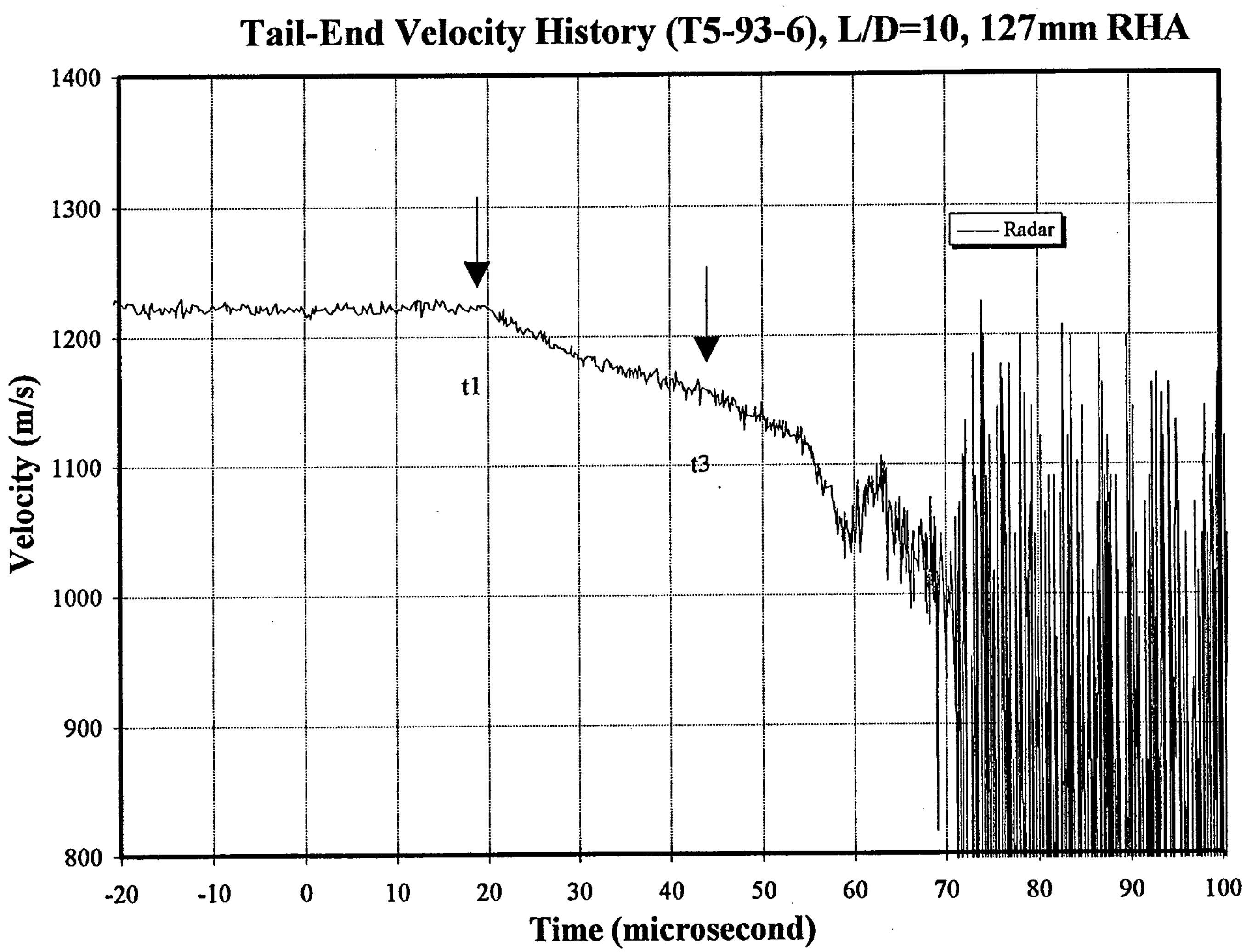

Figure 10. Tail-end velocity-step changes and corresponding time sequence marked (test T5-93-6)

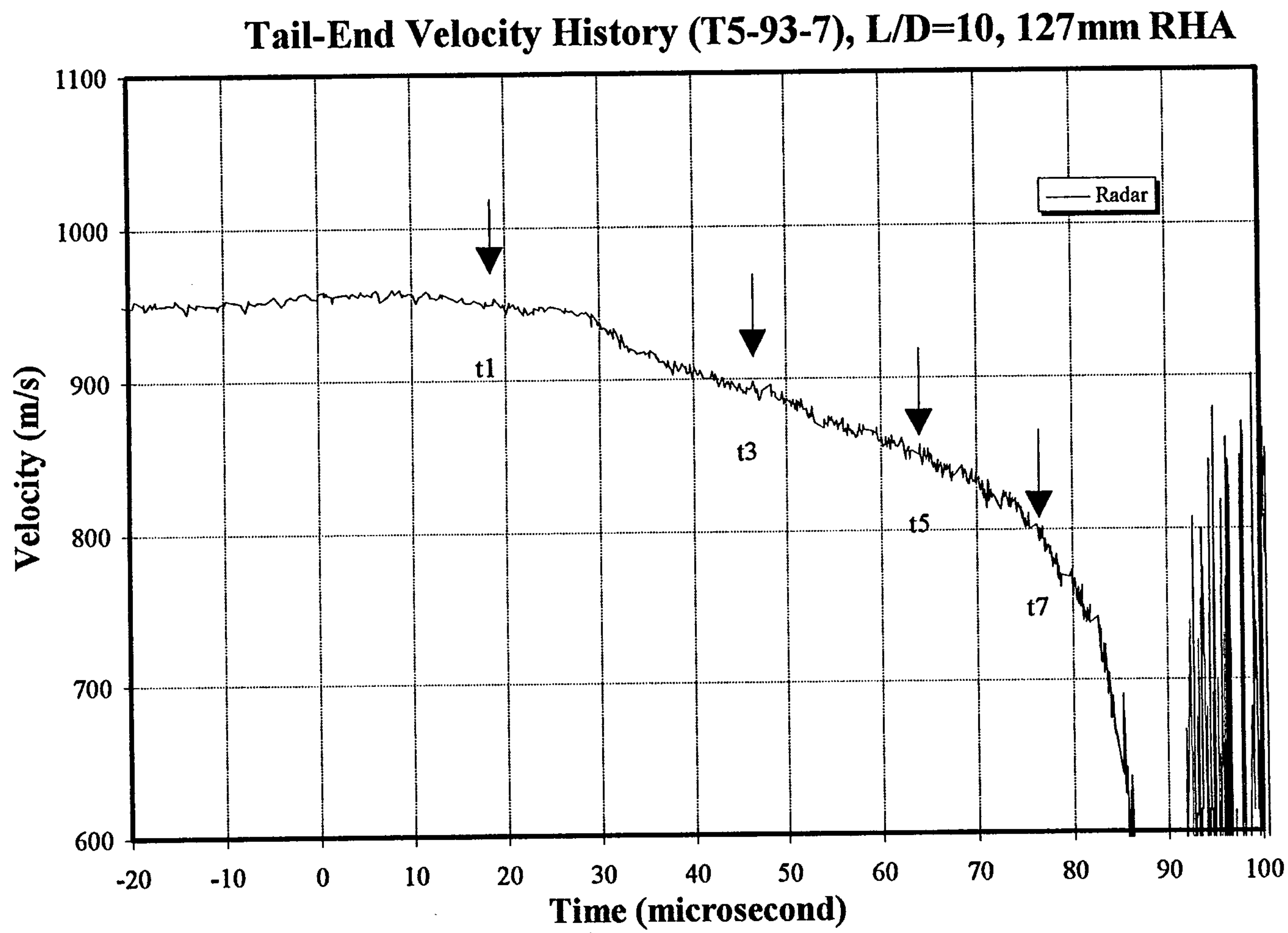

Figure 11. Tail-end velocity-step changes and corresponding time sequence marked (test T5-93-7)

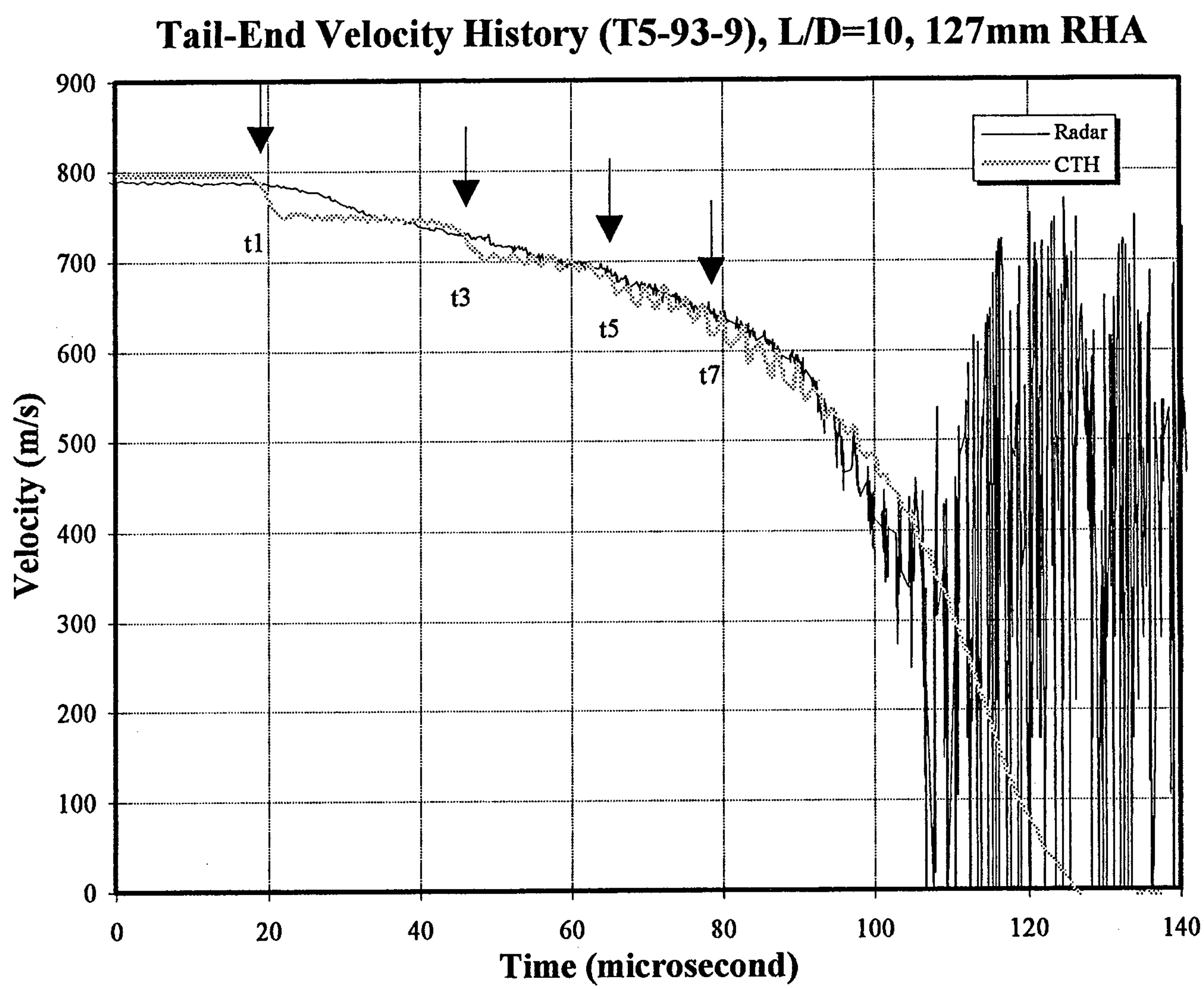

Figure 12. Tail-end velocity-step changes and corresponding time sequence marked (test T5-93-9). Dashed curve is the CTH calculation.

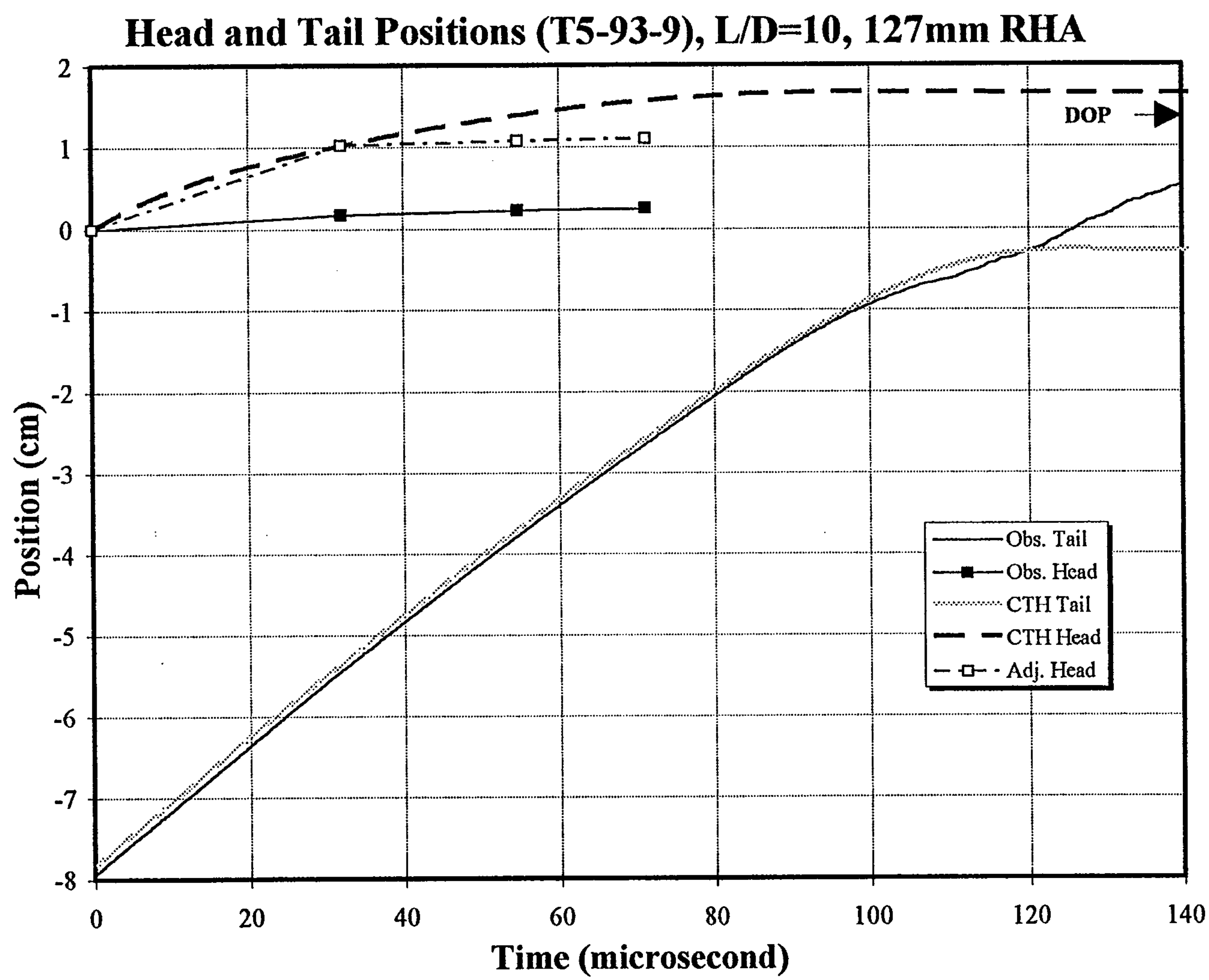

Figure 13. Head and tail positions history (test T5-93-9). Solid curves are from the measured tail-end velocity. Dashed curves are CTH calculations. Hollow squares represent estimated front-end positions when a 0.85-cm mushroom-head is added.

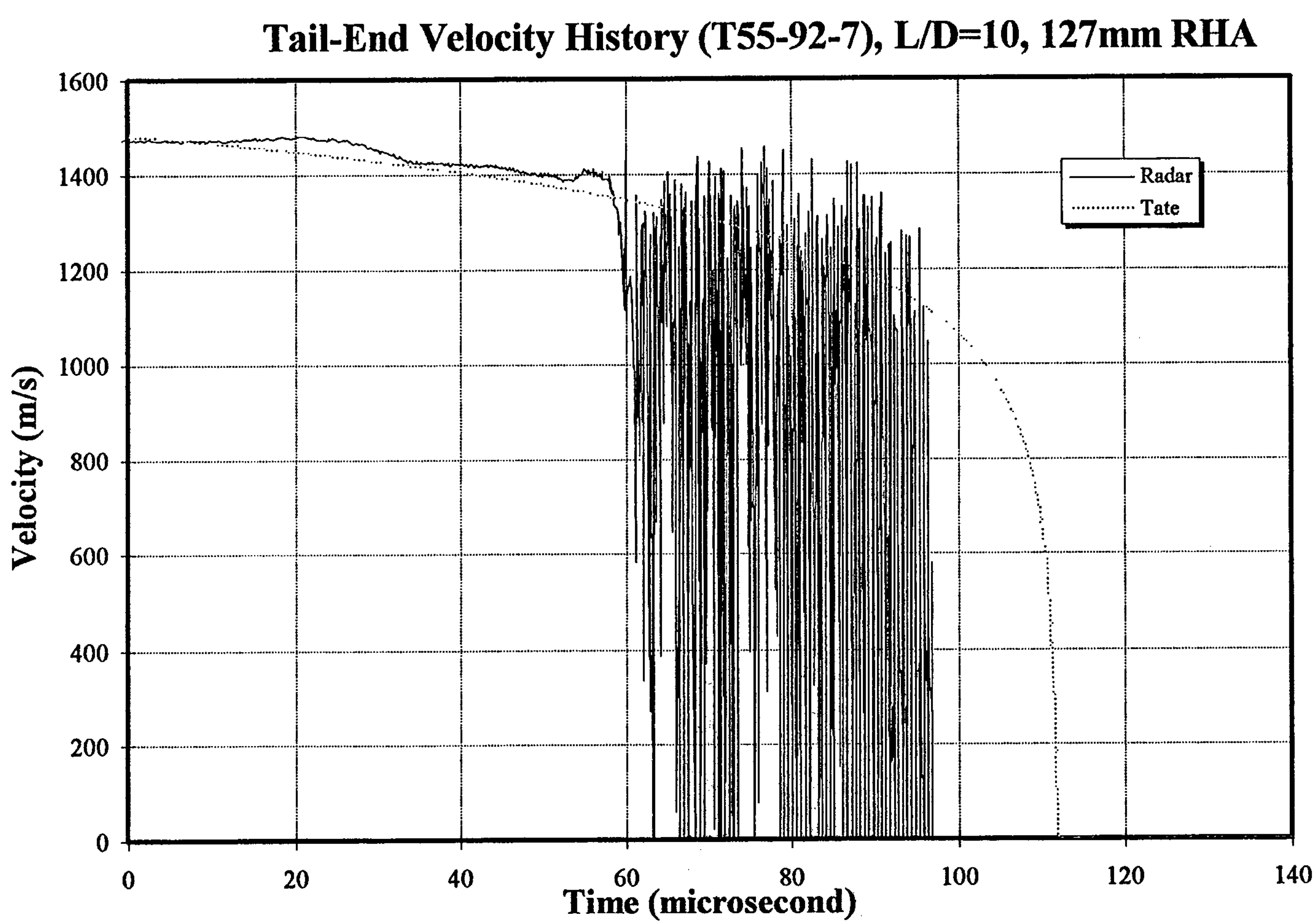

Figure 14. Tail-end velocity history for test T55-92-7 as compared to Tate model (the dashed curve)

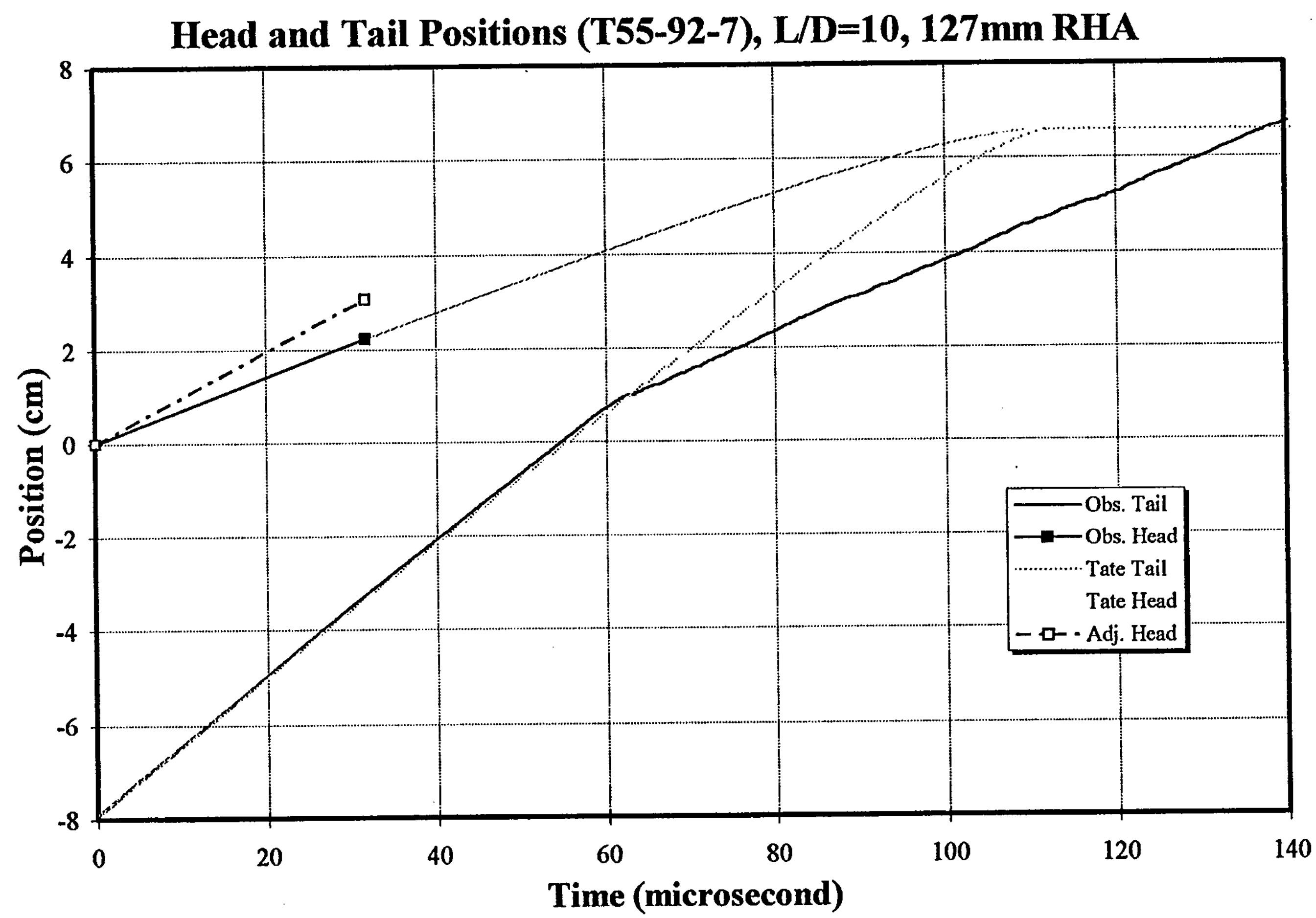

Figure 15. Head and tail positions history (test T55-92-7). Solid curves are from the measured tail-end velocity. Dashed curves are from Tate model. Hollow squares represent estimated front-end positions when a 0.85-cm mushroom-head is added.

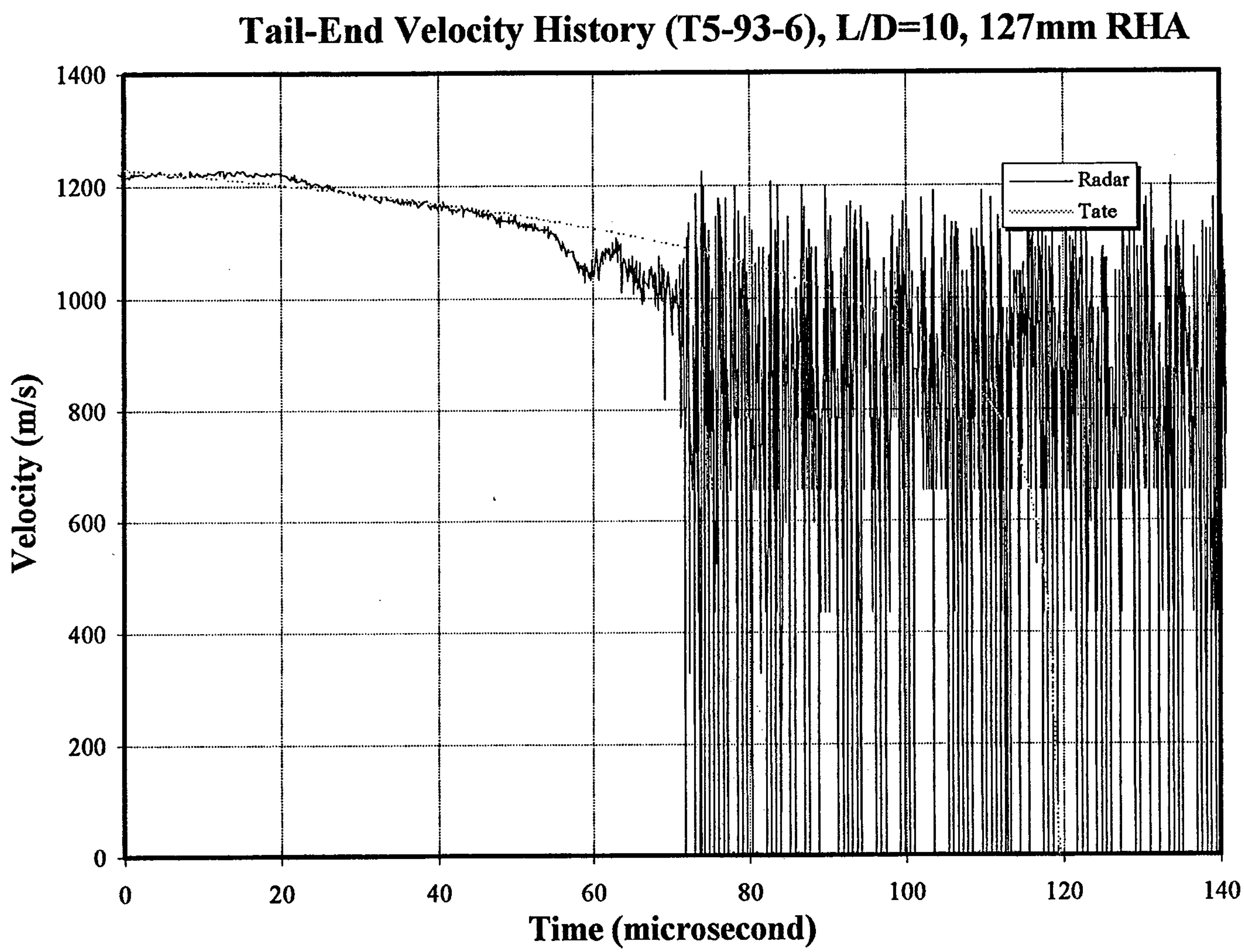

Figure 16. Tail-end velocity history for test T5-93-6 as compared to Tate model (the dashed curve)

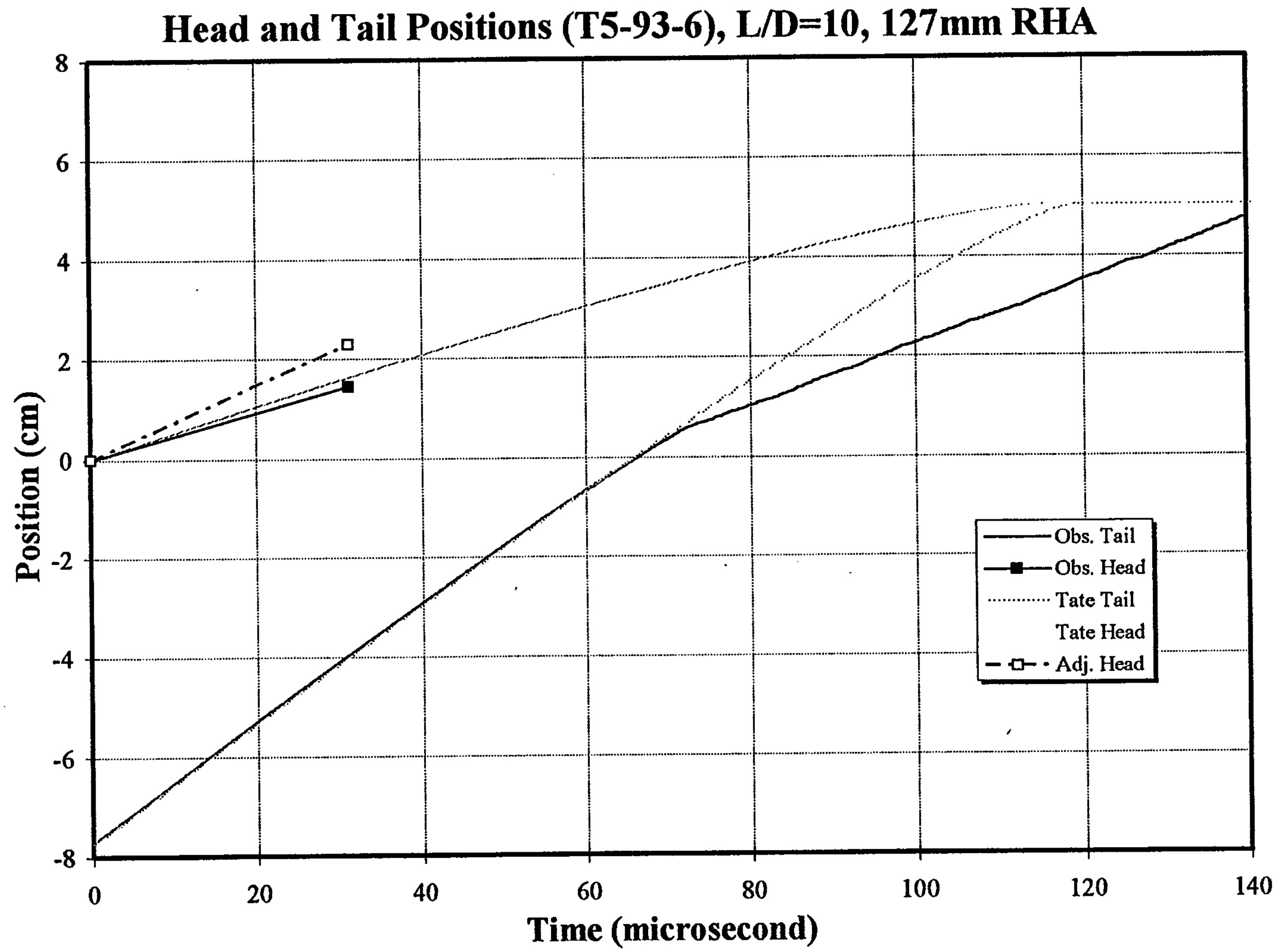

Figure 17. Head and tail positions history (test T5-93-6). Solid curves are from the measured tail-end velocity. Dashed curves are from Tate model. Hollow squares represent estimated front-end positions when a 0.85-cm mushroom-head is added.

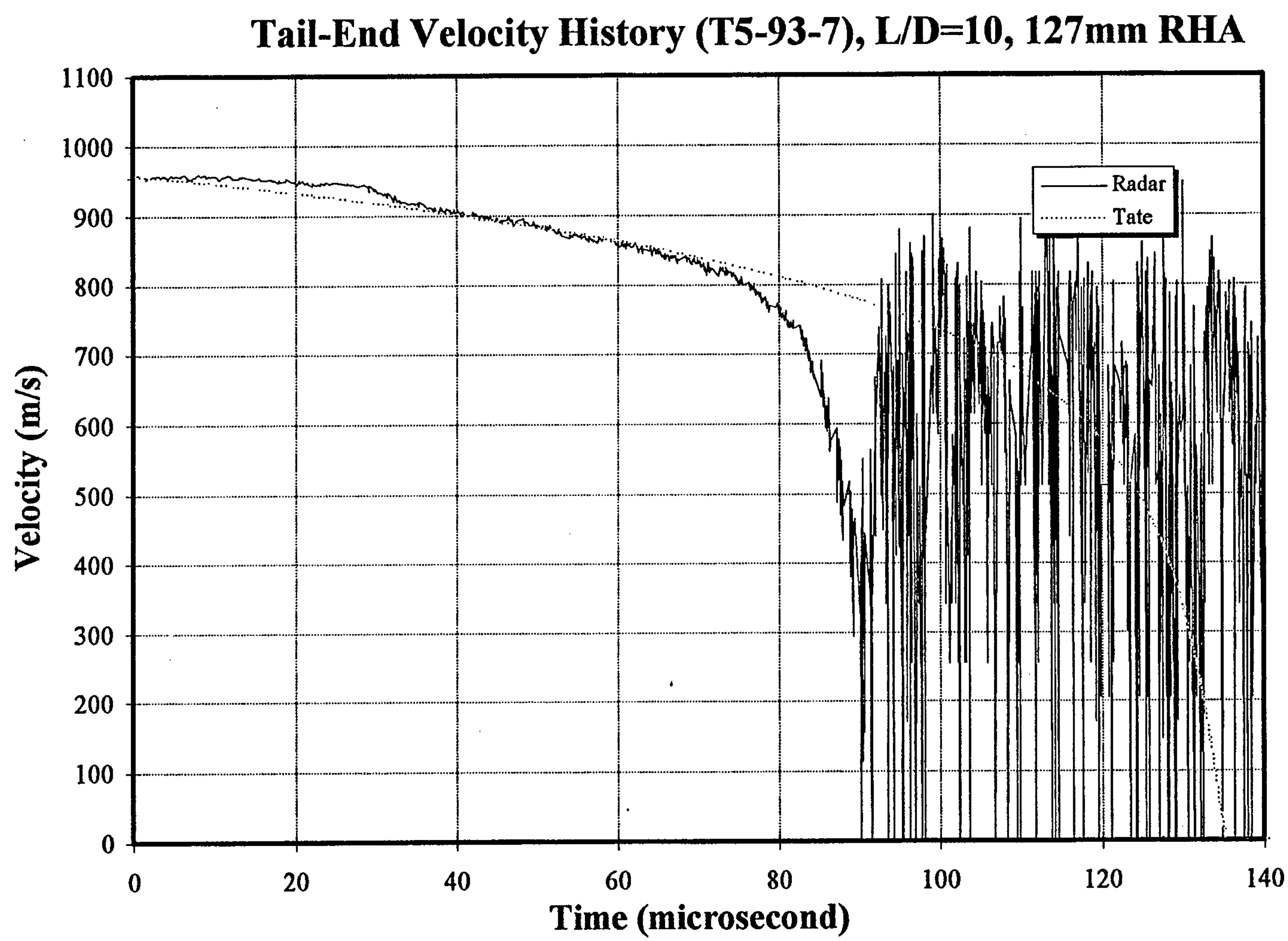

Figure 18. Tail-end velocity history for test T5-93-7 as compared to Tate model (the dashed curve)

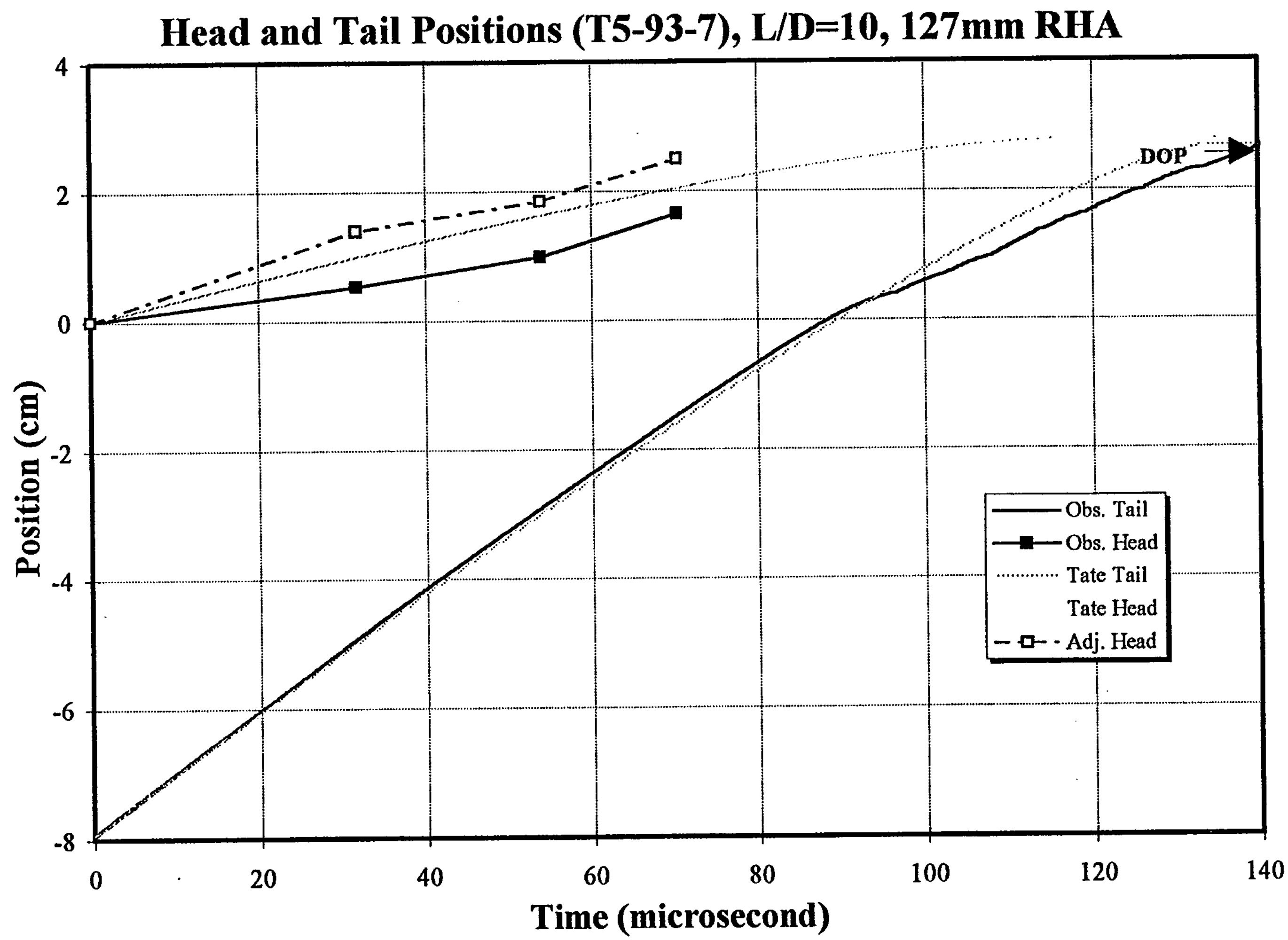

Figure 19. Head and tail positions history (test T5-93-7). Solid curves are from the measured tail-end velocity. Dashed curves are from Tate model. Hollow squares represent estimated front-end positions when a 0.85-cm mushroom-head is added.

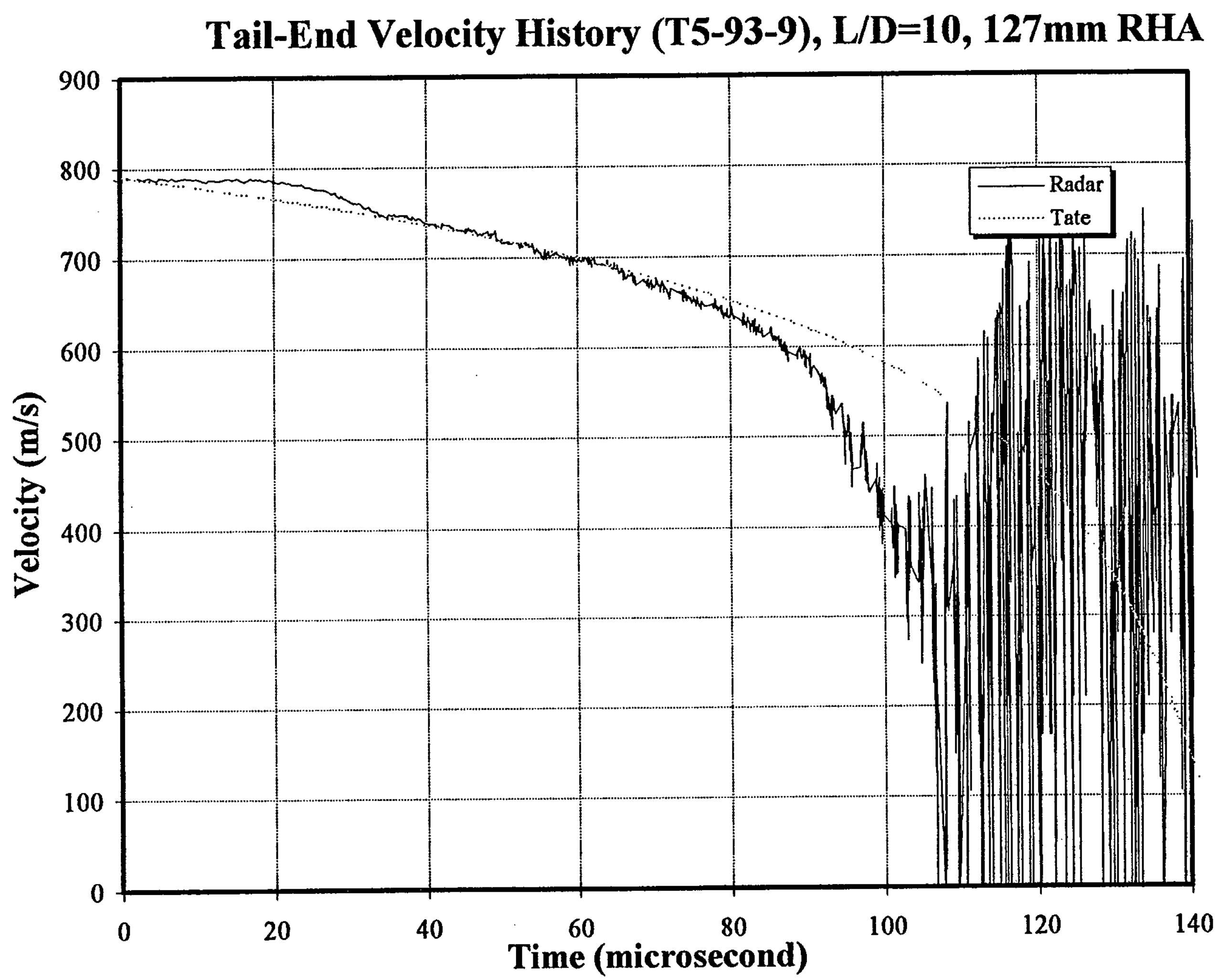

Figure 20. Tail-end velocity history for test T5-93-9 as compared to Tate model (the dashed curve)

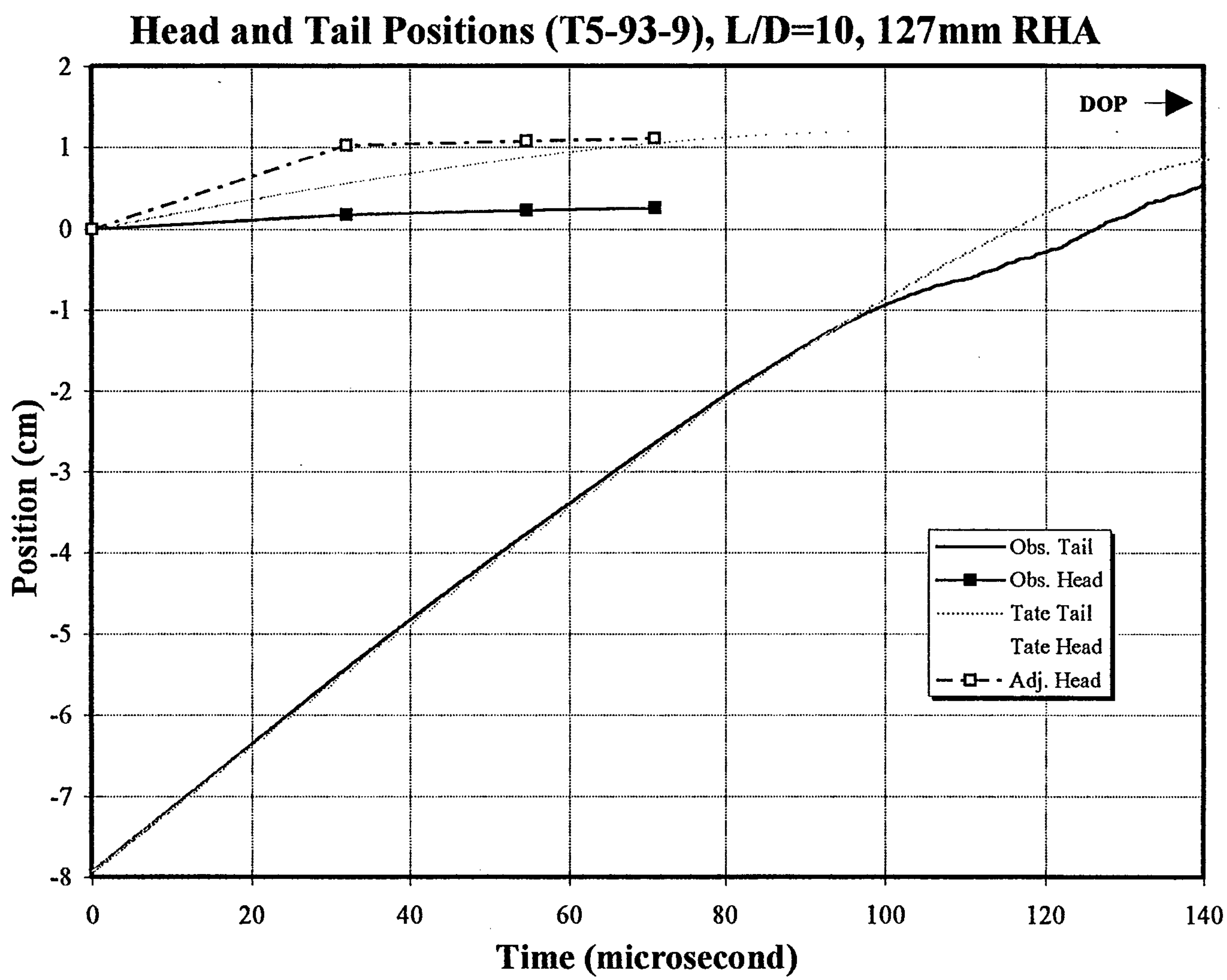

Figure 21. Head and tail positions history (test T5-93-9). Solid curves are from the measured tail-end velocity. Dashed curves are from Tate model. Hollow squares represent estimated front-end positions when a 0.85-cm mushroom-head is added.

NO. OF COPIES	ORGANIZATION
2	ADMINISTRATOR ATTN DTIC DDA DEFENSE TECHNICAL INFO CTR CAMERON STATION ALEXANDRIA VA 22304-6145
1	DIRECTOR ATTN AMSRL OP SD TA US ARMY RESEARCH LAB 2800 POWDER MILL RD ADELPHI MD 20783-1145
3	DIRECTOR ATTN AMSRL OP SD TL US ARMY RESEARCH LAB 2800 POWDER MILL RD ADELPHI MD 20783-1145
1	DIRECTOR ATTN AMSRL OP SD TP US ARMY RESEARCH LAB 2800 POWDER MILL RD ADELPHI MD 20783-1145
	<u>ABERDEEN PROVING GROUND</u>
2	DIR USARL ATTN AMSRL OP AP L (305)

NO. OF COPIES	ORGANIZATION
1	OUSA DR&E PENTAGON WASHINGTON DC 20301
1	DIRECTOR ATTN AMSRL OP CI AD TECHNICAL PUB BRANCH 2800 POWDER MILL RD ADELPHI MD 20783-1145
1	DIRECTOR ATTN AMSRL OP CI AD RECORDS MGMT ADMIN 2800 POWDER MILL RD ADELPHI MD 20783-1145
1	DIRECTOR USARL ATTN AMSRL SS 2800 POWDER MILL RD ADELPHI MD 20783-1145
1	COMMANDER ATTN AMXRO RT OFC RSRCH & TECH INTEGRATION PO BOX 12211 RESEARCH TRIANGLE PARK NC 27709-2211
1	COMMANDER ATTN AMXRO MS DR A CROWSON PO BOX 12211 RESEARCH TRIANGLE PARK NC 27709-2211
1	COMMANDER ATTN AMXRO EN DR KAILASAM IYER PO BOX 12211 RESEARCH TRIANGLE PARK NC 27709-2211
1	COMMANDER ATTN AMXRO MS DR JOHN BAILEY PO BOX 12211 RESEARCH TRIANGLE PARK NC 27709-2211
2	COMMANDER CAMERON STATION BLDG 5 ATTN DTIC-FDAC 5010 DUKE ST ALEXANDRIA VA 22304-6145

NO. OF COPIES	ORGANIZATION
1	COMMANDER ATTN AMCSCI DR R CHAIT 5001 EISENHOWER AVE ALEXANDRIA VA 22333-0001
1	COMMANDER US ARMY MISSILE CMD ATTN AMSMI RD ST DR L MIXON REDSTONE ARSENAL AL 35809
1	COMMANDER USA ARDEC ATTN SMCAR AET DR W EBIHARA PICATINNY ARSENAL NJ 07806-5000
1	COMMANDER USA NATICK RD&E CTR ATTN TECHNICAL LIBRARY NATICK MA 01760-5010
1	COMMANDER USA NATICK RD&E CTR ATTN STRNC ITFR T TASSINARI NATICK MA 01760-5010
1	COMMANDER USA NATICK RD&E CTR ATTN STRNC ICAA S WACLAWIK NATICK MA 01760-5010
1	COMMANDER USA TANK AUTO CMD ATTN AMSTA ZE WARREN MI 48397-5000
1	COMMANDER USA TANK AUTO CMD ATTN AMSTA TSL TECHNICAL LIBRARY WARREN MI 48397-5000
1	COMMANDER USA TANK AUTO CMD ATTN AMSTA RSK S GOODMAN WARREN MI 48397-5000

NO. OF COPIES	ORGANIZATION
1	COMMANDER USA TANK AUTO CMD ATTN AMSTA RS J THOMPSON WARREN MI 48397-5000
1	COMMANDER USA TANK AUTO CMD ATTN AMSTA RTC R BRYNSVALD WARREN MI 48397-5000
1	COMMANDER USA TANK AUTO CMD ATTN AMSTA RTC S KRAMER WARREN MI 48397-5000
1	COMMANDER USA TANK AUTO CMD ATTN AMSTA RTC D OSTBERG WARREN MI 48397-5000
1	COMMANDER USA TANK AUTO CMD ATTN AMSTA RSX D TENENBAUM WARREN MI 48397-5000
1	DIRECTOR DEFENSE INTELL AGCY ATTN ODT 5A F JAEGER WASHINGTON DC 20340-6053
1	COMMANDER EUROPEAN RESEARCH OFC USARDSG (UK) ATTN R REICHENBACH PSC 802 BOX 15 FPO AE 09499-1500
1	AIR FORCE ARMAMENT LABORATORY ATTN AFATL DLJW J FOSTER JR ELGIN AFB FL 32542-5434
1	AIR FORCE ARMAMENT LABORATORY ATTN AFATL DLJW W COOK ELGIN AFB FL 32542-5434

NO. OF COPIES	ORGANIZATION
1	NAVAL RESEARCH LAB ATTM DR R BADALIANCE CODE 6380 WASHINGTON DC 20375
2	NAVAL SURFACE WARFARE CTR ATTN F ZERILLI CODE R13 ATTN R GARRETT SILVER SPRING MD 20903-5000
3	SOUTHWEST RESEARCH INST ATTN DR C ANDERSON J RIEGEL J WALKER 6220 CULEBRA RD SAN ANTONIO TX 78238
1	DIRECTOR BENET WEAPONS LABS ATTN SMCAR CCB DR W KITCHENS WATERVLIET NY 12189-4050
1	DIRECTOR BENET WEAPONS LABS ATTN SMCAR CCB DR J VASILAKIS WATERVLIET NY 12189-4050
1	COMMANDER ATTN AIFRTC G SCHLESINGER APPL TECH BR 220 7TH ST NE CHARLOTTESVILLE VA 22901-5396
1	COMMANDANT USA QUARTERMASTER SCHOOL ATTN QUATERMASTER SCHOOL LIBRARY FT LEE VA 23801
1	INSTITUTE FOR ADV TECH ATTN S BLESS 4030 2 W BRAKER AUSTIN TX 78759-5329
2	SANDIA NATL LABS ATTN E CHEN DIV 1561 P YARRINGTON DIV 1533 PO BOX 5800 ALBURQUERQUE NM 87185

NO. OF COPIES	ORGANIZATION
1	ARPA MATLS SCI OFC ATTN B WILCOX 1400 WILSON BLVD ARLINGTON VA 22209-2308
1	ARPA TTO ATTN R KOCHER 3701 N FAIRFAX DR ARLINGTON VA 22203-1714
	ABERDEEN PROVING GROUND
38	DIR, USARL ATTN: AMSRL-MD-P, D. VIECHNICKI AMSRL-MD-PD, A. CHANG (20 CPS) S. CHOU D. DANDEKAR J. MACKIEWICZ R. RAJENDRAN AMSRL-WT, I. MAY AMSRL-WT-TA, W. BRUCHEY W. GOOCH G. GILBEY, JR. W. GILLICH E. RAPACKI, JR. M. ZOLTOSKI AMSRL-WT-TC, W. DEROSSET F. GRACE L. MAGNESS AMSRL-WT-TD, K. FRANK AMSRL-OP-WT-IS, TECH LIB (2)

USER EVALUATION SHEET/CHANGE OF ADDRESS

This Laboratory undertakes a continuing effort to improve the quality of the reports it publishes. Your comments/answers to the items/questions below will aid us in our efforts.

1. ARL Report Number/Author ARL-TR-1187 (Chang) Date of Report August 1996

2. Date Report Received ______

3. Does this report satisfy a need? (Comment on purpose, related project, or other area of interest for which the report will be used.) ______

4. Specifically, how is the report being used? (Information source, design data, procedure, source of ideas, etc.) ______

5. Has the information in this report led to any quantitative savings as far as man-hours or dollars saved, operating costs avoided, or efficiencies achieved, etc? If so, please elaborate. ______

6. General Comments. What do you think should be changed to improve future reports? (Indicate changes to organization, technical content, format, etc.) ______

CURRENT ADDRESS

Organization

Name

Street or P.O. Box No.

City, State, Zip Code

7. If indicating a Change of Address or Address Correction, please provide the Current or Correct address above and the Old or Incorrect address below.

OLD ADDRESS

Organization

Name

Street or P.O. Box No.

City, State, Zip Code

(Remove this sheet, fold as indicated, tape closed, and mail.)
(DO NOT STAPLE)

DEPARTMENT OF THE ARMY

OFFICIAL BUSINESS

NO POSTAGE NECESSARY IF MAILED IN THE UNITED STATES

BUSINESS REPLY MAIL
FIRST CLASS PERMIT NO 0001,APG,MD

POSTAGE WILL BE PAID BY ADDRESSEE

DIRECTOR
U.S. ARMY RESEARCH LABORATORY
ATTN: AMSRL-MA-PD
ABERDEEN PROVING GROUND, MD 21005-5069